Dysregulation of mitochondrial translation caused by CBFB deficiency cooperates with mutant PIK3CA and is a vulnerability in breast cancer

Navdeep Malik[1], **Young-Im Kim**[1], **Hualong Yan**[1], **Yu-Chou Tseng**[1], **Wendy du Bois**[2], **Gamze Ayaz**[1], **Andy D. Tran**[3], **Laura Vera-Ramirez**[4,5,6], **Howard Yang**[7], **Aleksandra M. Michalowski**[1], **Michael Kruhlak**[3], **Maxwell Lee**[7], **Kent W. Hunter**[4], **Jing Huang**[1,*]

[1]Cancer and Stem Cell Epigenetics Group, Laboratory of Cancer Biology and Genetics, Center for Cancer Research, National Cancer Institute, Bethesda, MD, USA

[2]Animal Model and Genotyping Facility, Laboratory of Cancer Biology and Genetics, Center for Cancer Research, National Cancer Institute, Bethesda, MD, USA

[3]CCR Microscopy Core Facility, Laboratory of Cancer Biology and Genetics, Center for Cancer Research, National Cancer Institute, Bethesda, MD, USA

[4]Metastasis Susceptibility Group, Laboratory of Cancer Biology and Genetics, Center for Cancer Research, National Cancer Institute, Bethesda, MD, USA

[5]Department of Genomic Medicine, GENYO: Centre for Genomics and Oncology (Pfizer-University of Granada and Andalusian Regional Government), PTS, Granada, Spain

[6]Department of Physiology, Institute of Nutrition and Food Technology "José Mataix Verdú", Biomedical Research Center, University of Granada, Granada, Spain

[7]High-dimension Data Analysis Group, Laboratory of Cancer Biology and Genetics, Center for Cancer Research, National Cancer Institute, Bethesda, MD, USA

Abstract

Understanding functional interactions between cancer mutations is an attractive strategy for discovering unappreciated cancer pathways and developing new combination therapies to improve personalized treatment. However, distinguishing driver gene pairs from passenger pairs remains challenging. Here, we designed an integrated omics approach to identify driver gene pairs by leveraging genetic interaction analyses of top mutated breast cancer genes and the proteomics interactome data of their encoded proteins. This approach identified that PIK3CA oncogenic gain-of-function (GOF) and CBFB loss-of-function (LOF) mutations cooperate to promote breast tumor progression in both mice and humans. The transcription factor CBFB localized to

[*], corresponding author, Jing Huang, Ph.D., huangj3@mail.nih.gov, 37 Convent Dr. Building 37, Room 3140A, Bethesda, MD 20814.

Conflict of interest disclosure statement
K. Hunter is an editorial board member of *Cancer Research*. The other authors declare no potential conflicts of interest.

mitochondria and moonlighted in translating the mitochondrial genome. Mechanistically, CBFB enhanced the binding of mitochondrial mRNAs to TUFM, a mitochondrial translation elongation factor. Independent of mutant PI3K, mitochondrial translation defects caused by CBFB LOF led to multiple metabolic reprogramming events, including defective oxidative phosphorylation (OXPHOS), the Warburg effect, and autophagy/mitophagy addiction. Furthermore, autophagy and PI3K inhibitors synergistically killed breast cancer cells and impaired the growth of breast tumors, including patient-derived xenografts (PDXs) carrying CBFB LOF and PIK3CA GOF mutations. Thus, our study offers mechanistic insights into the functional interaction between mutant PI3K and mitochondrial translation dysregulation in breast cancer progression and provides a strong preclinical rationale for combining autophagy and PI3K inhibitors in precision medicine for breast cancer.

Introduction

Mutations in tumors often collaborate to control pathways underlying the hallmark features of cancer cells. Due to the functional interaction of collaborative gene mutations, targeting a single pathway or gene product often has heterogeneous responses in tumors. For instance, the *PIK3CA* gene is mutated in 30-40% of breast tumors, but PIQRAY (Alpelisib, BYL719), the first-in-class inhibitor of mutant PIK3CA, is only effective in a fraction of patients with *PIK3CA* mutant tumors (1). Thus, identifying druggable, functionally interacting mutant pairs is critical for elucidating unappreciated cancer pathways and developing combination therapies to improve precision oncology. One approach is to use unbiased drug screening in cell lines by combining known drugs (2). Although powerful, the number of possible cancer gene pairs is still far beyond the testing capacity of screening. Another complementary approach is to perform integrated multi-omics analyses by leveraging genomics, epigenomics, and proteomics datasets. As orthogonal datasets become more available, this approach has the potential to yield valuable insights into the functional interaction of cancer gene pairs in cancer progression.

In this report, we use breast cancer as a model and integrate genetic interaction data of top mutated genes with proteomic interacting data of the protein products of these genes. These integrated analyses reveal that mutations in the phosphoinositide 3-kinase (PI3K) pathway and core binding factor beta (CBFB) functionally interact. Using xenografts and genetically engineered mouse models (GEMMs), we provide compelling evidence that CBFB loss-of-function (LOF) mutations and PIK3CA oncogenic gain-of-function (GOF) mutations cooperatively promote breast tumor progression. Mechanistic studies reveal that, in addition to its roles in other cellular compartments, CBFB moonlights as a major regulator of mitochondrial translation. Consequently, dysregulation of mitochondrial translation through CBFB LOF is a common event in the metabolic reprogramming of breast cancer cells, rendering these cancer cells dependent on autophagy/mitophagy for survival. Moreover, preclinical data show that mitochondrial translation dysregulation through CBFB LOF is therapeutically targetable by combining autophagy and PIK3CA inhibitors. Our results highlight the importance of CBFB-regulated mitochondrial translation in breast tumor progression and provide a strong preclinical rationale for combining autophagy and PIK3CA inhibitors in breast cancer precision oncology.

Materials and Methods

Reagents

MCF10A cell culture components; hydrocortisone (Cat#H0888g), recombinant human insulin (Cat#910077C), and cholera toxin (Cat#C8052) were purchased from Sigma. Human epidermal growth factor (EGF) was procured from PeproTech (Cat#AF100-15). Hydroxychloroquine sulfate (HCQ, Cat#PHR1782) and BYL719 (Cat# HY-15244) were purchased from Sigma and MedChemExpress, respectively. ULK inhibitors; SBI-0206965 (Cat#18477) and MRT68921 (Cat#19905) were procured from Cayman.

For immunoblotting, the following antibodies were used: CBFB (Thermo Fisher Scientific Cat# A303-547A, RRID:AB_10953532, 1:1000), hnRNPK (Bethyl Cat# A300-674A, RRID:AB_530277, 1:1000), PIK3CA (PI3 Kinase p110α, (Cell Signaling Technology Cat# 4249, RRID:AB_2165248), 1:1000), COX IV (Cell Signaling Technology Cat# 4850, RRID:AB_2085424), 1:1000), MT-CO2 (Bethyl Cat# A305-318A, RRID:AB_2631711), 1:2000), MT-CYB (Abcam, Cat# Ab219823, RRID:AB_2928084, 1:1000), MT-ATP6 (Millipore, Cat# MABS1995, RRID:AB_2928083, 1:500), estrogen receptor α (Cell Signaling Technology Cat# 8644, RRID:AB_2617128, 1:1000), phospho-AKT (Ser473) (Cell Signaling Technology Cat# 4060, RRID:AB_2315049, 1:1000), AKT (pan) (Cell Signaling Technology Cat# 4691, RRID:AB_915783, 1:1000), alpha-tubulin (Cell Signaling Technology Cat# 2144, RRID:AB_2210548, 1:1000), HSP60 (Cell Signaling Technology Cat# 12165, RRID:AB_2636980, 1:1000), Cytochrome c (Cell Signaling Technology Cat# 11940, RRID:AB_2637071, 1:1000), Phospho-ULK1-S555 (Cell Signaling Technology Cat# 5869, RRID:AB_10707365, 1:1000), Phospho-ULK1-S757 (Cell Signaling Technology Cat# 6888, RRID:AB_10829226, 1:1000), ULK1 (Cell Signaling Technology Cat# 8054, RRID:AB_11178668, 1:1000), Phospho-AMPK-T172 (Cell Signaling Technology Cat# 2535, RRID:AB_331250, 1:1000), AMPK1 (Bethyl Cat# A300-507A, RRID:AB_155884, 1:5000), LC3A/B (Cell Signaling Technology Cat# 12741, RRID:AB_2617131, 1:1000), β-actin (Sigma-Aldrich Cat# A5316, RRID:AB_476743, 1:5000), H3 (Millipore Cat# 07-690, RRID:AB_417398, 1:5000), and GAPDH (Abcam Cat# ab9484, RRID:AB_307274, 1:5000).

For immunohistochemistry (IHC), the following antibodies were used: Ki67 (Cell Signaling Technology Cat# 12202, RRID:AB_2620142, 1:200), ERα (Santa Cruz Biotechnology Cat# sc-542, RRID:AB_631470, 1:250), PR (Agilent Cat# A0098, RRID:AB_2315192, 1:200), LC3A/B ((Cell Signaling Technology Cat# 12741, RRID:AB_2617131, 1:100), CBFB (Bethyl Cat# A303-549A, RRID:AB_10951838, 1:1000), TUFM (Abcam Cat# ab173300, RRID:AB_2750903, 1:100), PIK3CA (PI3 Kinase p110α, (Cell Signaling Technology Cat# 4249, RRID:AB_2165248, 1:100) and MT-CO1 (Abcam Cat# ab14705, RRID:AB_2084810, 1:100).

For immunofluorescence (IFC), the following antibodies were used: CBFB (Bethyl Cat# A303-549A, RRID:AB_10951838, 1:1000 or Santa Cruz, (Santa Cruz Biotechnology Cat# sc-56751, RRID:AB_781871, 1:100), LAMP1 (Cell Signaling Technology Cat# 9091, RRID:AB_2687579, 1:200), TUFM (Abcam Cat# ab173300, RRID:AB_2750903, 1:100), MT-CO1 (Abcam Cat# ab14705, RRID:AB_2084810, 1:100), COX IV (Abcam

Cat# ab33985, RRID:AB_879754, 1:200), PIK3CA (PI3 Kinase p110α, (Cell Signaling Technology Cat# 4249, RRID:AB_2165248, 1:100), and hnRNPK (Bethyl Cat# A300-674A, RRID:AB_530277, 1:1000). For RNA immunoprecipitation (RIP), the following antibodies were used: CBFB (Bethyl Cat# A303-549A, RRID:AB_10951838, 1 μg), hnRNPK (Bethyl Cat# A300-674A, RRID:AB_530277, 1 μg), and TUFM (Bethyl Cat# A305-014A, RRID:AB_2621208, 1 μg). For PLA, TUFM (Abcam Cat# ab173300, RRID:AB_2750903, 1:100) and CBFB (Santa Cruz Biotechnology Cat# sc-56751, RRID:AB_781871, 1:100) antibodies were used. For immunoprecipitation (IP), CBFB (Bethyl Cat# A303-549A, RRID:AB_10951838, 1 μg) antibody was used.

Cell culture

MCF10A (Cat#CRL-10317, RRID:CVCL_0598), MCF7 (Cat# HTB-22, RRID:CVCL_0031), BT474 (Cat# HTB-20, RRID:CVCL_0179), and MDA-MB-361 (Cat#HTB-27, CVCL_0620) cell lines were procured from ATCC (Manassas, VA). All cell lines used in this study were tested every two months and confirmed to be mycoplasma free using the MycoAlert™ Mycoplasma Detection Kit (Lonza, Cat#LT07-218). MCF7 cells were grown in Eagle's Minimum Essential Medium (EMEM) supplemented with 10% FBS, 10 μg/ml human recombinant insulin, and antibiotics. MCF10A cells were cultured in DMEM/F12 supplemented with 5% horse serum, 20 ng/ml human EGF, 500 ng/ml hydrocortisone, 10 μg/ml human recombinant insulin, 100 ng/ml Cholera toxin, and antibiotics. All other cell lines were cultured in DMEM supplemented with 10% FBS and antibiotics. All cell lines were maintained in an incubator set at 37°C and supplied with 5% CO_2 and less than passage 20.

Bioinformatic analyses

For RIP-seq and eCLIP, public datasets were re-analyzed: CBFB and hnRNPK RIP-seq (GSE8834172), hnRNPK eCLIP (GSM2423241). Raw data were downloaded from the SRA archive and aligned to hg38 using STAR. BigWig files were generated using the bamCompare module in deepTools (ver 3.5.0).

RNA immunoprecipitation (RIP) assay

RIP assays were performed as previously described (3). Briefly, the dounce method was used to prepare clear cell lysate. 1 μg of antibody was incubated overnight with 500 μg of cell lysate at 4°C. The next day, protein A agarose beads were added to the lysate, which was then incubated for an additional 4 hours at 4°C. Finally, beads were washed with RPA buffer (50 mM Tris, pH 7.5, 250 mM KCl, 5 mM EDTA, 0.5 mM DTT, 1% NP40 plus protease inhibitors and RNase inhibitors), and total RNA was extracted using Trizol (Invitrogen) and analyzed by real-time PCR.

Immunofluorescence staining, confocal microscopy, and super-resolution microscopy

Immunofluorescence was performed as described previously (4). Briefly, 1x105 cells were plated overnight in a Lab-Tek II chamber slide (2 well, Nunc, Cat# MitoTracker Red (Fisher Scientific 155380). The next day, cells were fixed with 4% formaldehyde and blocked with buffer (5% normal goat serum+0.3% Triton X-100 in 1X PBS) for 1

hour at room temperature (RT). Subsequently, cells were incubated overnight in primary antibodies at 4°C. The next day, cells were extensively washed with PBS followed by incubation with secondary antibodies conjugated to either Alexa Fluor 488 or Alexa Fluor 568 (Thermo Fisher Scientific Cat# A-11001, RRID:AB_2534069, Thermo Fisher Scientific Cat# A-11008, RRID:AB_143165 , Thermo Fisher Scientific Cat# A-11011, RRID:AB_143157, or Thermo Fisher Scientific Cat# A-11031, RRID:AB_144696) for 2 hours. After incubation, cells were washed with PBS and incubated with DAPI (1:2000) for 1 hour at RT for nuclei visualization. After staining, cells were washed and mounted with VECTASHIELD® mounting media (Vector Laboratories, Inc Burlingame, CA). Confocal microscopy of stained cells was performed using a Zeiss LSM 780 microscope with either a 63x plan-apochromat (N.A. 1.4) or 100x plan-apochromat (N.A. 14.) oil immersion objective lens. For MitoTracker Green (Fisher Scientific, Cat#M7514) or MitoTracker Red (Fisher Scientific, Cat#M22425) staining, cells were stained as per the manufacturer's instructions.

For quantification of mitophagy using machine learning: confocal images were acquired with a Zeiss LSM880 microscope using a 63x plan-apochromat oil immersion objective lens (N.A. 1.4), 0.09 mm x-y pixel size and 0.9 mm optical section thickness (Carl Zeiss Microscopy, Inc., Thornwood, NY). Images were exported as OME-TIFF and processed using a Denoise.ai algorithm in Nikon Elements software (v 5.2) (Nikon Instruments, Inc., Melville, NY). The denoised images were then analyzed using Python-based image analysis algorithms. Briefly, mitophagy in COX IV- and LAMP1-stained images was quantified using the Python packages *scikit-image* and *scikit-learn* (5). Whole cells were segmented using marker-based watershed segmentation, using nuclei maxima as seed points. LAMP1-stained lysosomes were also segmented using marker-based watershed segmentation but using local LAMP1 intensity maxima as seed points. COX IV-stained mitochondria were segmented using a Random Forest machine learning pixel classifier. Object-object co-localized area was calculated by measuring the area of overlap between segmented mitochondria and segmented lysosomes. The mitophagy index was defined as the co-localized area multiplied by LAMP1 fluorescence intensity.

Super-resolution images were acquired with a Nikon SoRa spinning disk microscope using a 60x apo-TIRF oil immersion objective lens (N.A. 1.49) and Photometrics BSI sCMOS camera. Z-stacks were collected with 0.15 μm step size and were deconvolved in the Nikon Elements software (v. 5.3) using a modified Richardson-Lucy iterative deconvolution algorithm. The deconvolved images were imported into Imaris (v. 9.8.2) image analysis software for volume rendering and segmentation.

Electron microscopy

Wild-type (WT) and CBFB knockout (CBFB_KO) cells in the form of adherent cells in two wells of six well-plate were fixed with 2% glutaraldehyde in 0.1M Na Cacodylate buffer for an hour at room temperature for Transmission electron microscopy (TEM) processing. Two wells containing WT and CBFB_KO washed with 0.1M Na Cacodylate buffer two times for 10 min. After the second buffer wash, these cells were post fixed with 1% Osmium Tetroxide for an hour in the dark. After an hour post fixation, these cells were washed with

0.1M Na Cacodylate buffer twice for 10 min, and then washed once with 0.1N Na Acetate buffer and stained with 0.5% Uranyl Acetate for an hour in the dark. After en block staining, these cells were washed with 0.1N Na Acetate buffer twice for 10 min. After the last buffer wash, these cells were subjected to gradual dehydration in the order of 35%, 50%, 70% and 95% Ethanol twice each step for 10 min and three times with 100% Ethanol for 10 min. After the last step of 100% Ethanol rinse, these cells were infiltrated in 100% pure epoxy resin at room temperature overnight.

The next day, each well was washed with 100% pure epoxy resin twice and transferred to a 55 °C oven for 48 hours for polymerization. Epoxy resin (PolyScience Resin) ingredients consisted of a mixture of Poly/Bed 812 embedding Media, Dodecenylsuccinic Anhydride (DDSA), Nadic Methyl Anhydride (NSA) and DMP-30 to solidify the resin. After 48 hours, these cells in two wells of 6-well plate were taken out of the oven, and ultra-thin sectioned with a UC6 Leica Microtome at 75 nm. The ultra-thin sections were picked up on a 150 Copper mesh grid and were examined under a Hitachi H7600 Transmission electron microscope. The grids were post stained with 1:1 0.5% Uranyl Acetate in ddH2O and 70% Ethanol for 2 min and then rinsed with ddH2O for four times, then stained with 1:1 Lead Citrate and H2O for 2 min and rinsed with ddH2O four times. The grids were carbon coated with a TedPella/Cressington Evaporator and imaged in a Hitachi H7600 transmission electron microscope at 80KeV.

Mitochondria fractionation

Cellular mitochondria were fractionated using Mitochondria Isolation Kit for Cultured Cells (Abcam, Cat# ab110170) by following instructions from the manufacturer.

BIOID2

Stable CBFB KO MCF10A cell lines expressing retroviral expression plasmids, mycBioID2-pBabe-puro (EV, RRID:Addgene_80900) and mycBioID2-CBFB-pBabe-puro, were generated using a retroviral transduction system. Briefly, 2 million Platinum-A (Plat-A) cells were grown on a collagen-coated 60 mm dish in DMEM, 10% FBS media without any antibiotics. The next day, cells were transfected with 3 μg of the above-mentioned retroviral expression plasmids along with 150 μl of Opti-MEM and 9 μl of FuGENE transfection reagent (Promega, Cat# E2311). Retroviral supernatant was harvested 48 hours after transfection. 500 μl of retroviral supernatant, 1500 μl of DMEM/F12 media, and 6 μg/ml polybrene were used to transduce CBFB_KO MCF10A cells. Subsequently, cells were transferred to media containing 2 μg/ml puromycin to generate stable cell lines expressing mycBioID2-CBFB or the empty vector. For biotin pull-down, 8 million cells were grown in four 10-cm dishes, harvested, washed 2X with PBS, and lysed in 2 ml of lysis buffer (50 mM Tris pH 7.4, 500 mM NaCl, 0.4% SDS, 2% Triton X-100, 1 mM DTT, 5 mM EDTA, and protease inhibitors). Subsequently, cell lysates were sonicated for 5 min with 30 sec ON and 30 sec OFF using a Bioruptor sonicator. Next, the sonicated lysate was centrifuged at 13000 rpm and the supernatant was collected for protein estimation. 4 mg of protein from each sample was incubated with 150 μl of streptavidin magnetic beads (New England Biolabs, Cat# S1420S) overnight at 4°C with mixing. The next day, beads were collected using a magnetic stand and washed twice with 2% SDS for 10 minutes, followed

by 1X wash with 0.1% sodium deoxycholate, 1% Triton X-100, 500 mM NaCl, 1 mM EDTA, and 50 mM HEPES pH 7.5 for 10 minutes. Next, beads were washed 1X with 250 mM LiCl, 0.5% NP-40, 0.5% sodium deoxycholate, 1 mM EDTA and 10 mM Tris pH 8.0 for 10 minutes followed by 2X wash with 50 mM Tris pH 7.4, 150 mM NaCl for 5 minutes each. Finally, beads were washed once with 25 mM HEPES pH 7.3 for 5 minutes and resuspended in 100 μl of 25 mM HEPES and sent to the NCI Protein Laboratory for mass spectrometry analysis. The total number of identified peptides (peptide spectrum matches) for a specific protein was used to calculate the enrichment.

Proximity ligation assay (PLA)

PLA was performed using the Duolink In Situ Red Starter kit (Sigma, Cat#DUO92101) according to the manufacturer's instructions. Briefly, 2.5×10^4 cells were grown on a Millicell EZ slide (Sigma, Cat#PEZGS0816) for 48 hours. For formalin-fixed paraffin-embedded (FFPE) sections, antigen retrieval was performed using sodium citrate at sub-boiling temperature for 30 minutes. For PLA labeling, cells were fixed with 4% paraformaldehyde in PBS for 15 minutes, permeabilized with 0.3% Triton X-100 for 10 minutes, and then blocked with Duolink blocking solution at 37 °C for 1 hour. Samples were subsequently probed with the primary antibodies overnight at 4°C. Ligation and amplification of probes were performed per the manufacturer's instructions. Images were captured using the Zeiss LSM780 confocal microscope described above.

In situ mitochondrial translation assay

The assay was performed as described previously (6). Briefly, 2×10^5 cells were plated overnight on glass coverslips in complete DMEM/F12 media. The next day, cells were transferred to a methionine-free complete DMEM/F12 media (Caisson Labs, Cat: DFP14-10X1LT) with 5% dialyzed horse serum. The cytosolic translation was blocked by treating cells with cycloheximide (50 μg/ml, Research Product International, Cat # C81040-10) for 20 minutes. For the negative control set, cells were treated with cycloheximide (50 μg/ml) and chloramphenicol (150 μg/ml) for 50 minutes to block mitochondria protein translation. Subsequently, cells were labeled with 500 μM L-Homopropargylglycine (HPG, Sigma Cat #900893) for 30 minutes. After labeling, cells were incubated on ice for 2 minutes in buffer A [10 mM HEPES, 10 nM NaCl, 5 mM KCl, 300 mM sucrose, and 0.015% (w/v) digitonin] followed by 15 seconds of incubation in buffer A without digitonin. Afterward, coverslips were fixed in 4% paraformaldehyde in PBS for 30 minutes at room temperature. Subsequently, cells were washed in PBS for 5 minutes and quenched in 100 mM NH_4Cl in PBS for 15 minutes. Afterward, cells were washed three times (5 minutes each) in staining solution (PBS containing 5% BSA, 5% tryptone, and 0.1% Triton X-100). Next, coverslips were briefly washed in 3% BSA and clicked with Click-iT™ Cell Reaction Buffer Kit (Thermo Fisher, Cat #C10269) and 3 uM AZDye 594 Azide (Click Chemistry Tools, Cat#1295-1) for 20 minutes at room temperature. Cells were incubated in primary COX IV antibody (Abcam, Cat#ab33985) for 1 hour at room temperature after a quick wash with 3% BSA. Subsequently, cells were washed three times in staining solution and incubated for 1 hour at room temperature in secondary antibody (goat anti-mouse Alexa Fluor 488, Jackson ImmunoResearch Laboratory, Cat: 115-547-003) along with DAPI. Finally, cells were washed for 5 minutes

with PBS containing 5% BSA, 5% tryptone, followed by 5 minutes wash with high-salt PBS (PBS+500 mM NaCl) and a final wash with PBS before mounting and imaging at the Zeiss LSM780 confocal microscope.

Mitochondria protein translation assay in extracted mitochondria

The assay was performed as described previously (6). Briefly, 2×10^7 WT and CBFB_KO MCF10A cells were plated in complete DMEM/F12 media. The next day, cells were transferred to a methionine-free complete DMEM/F12 media with 5% dialyzed horse serum. The cytosolic translation was blocked by treating cells with cycloheximide for 20 minutes. For the negative control, cells were treated with both cycloheximide (50 μg/ml) and chloramphenicol (150 μg/ml) for 50 minutes to block mitochondria protein translation. Subsequently, cells were labeled with 500 μM L-Homopropargylglycine for 4 hours. After incubation, were extracted using the Mitochondria Isolation Kit for Cultured Cells (Abcam, Cat# ab110170) as per the manufacturer's instructions. Next, 70 μg of mitochondria protein lysate was click-labeled with 40 μM AZDye 594 Azide using Click-&-Go™ Protein Reaction Buffer Kit (Click Chemistry Tools, Cat#1262) as per the manufacturer's instructions. Subsequently, lysates were run on a NuPAGE gel, and the gel was scanned at FLA-6500 Starion (Fujifilm) to visualize fluorescent proteins.

Mitochondria Stress Test and Glycolysis Stress Test

Mitochondria Stress Tests (Agilent, 103015-100) and Glycolysis Stress Tests (Agilent Technologies, 103020-100) were performed as described previously (7). Briefly, 20,000 cells were plated onto a XF24 cell culture plate, followed by replacing the culture media with Agilent Seahorse XF Base Medium (Agilent, Cat#103334-100) supplemented with 2 mM glutamine (Sigma, Cat#G8540) for the Glycolysis Stress Tests, or with 1 mM sodium pyruvate (Sigma, Cat#S8636), 2 mM glutamine (Sigma, Cat#G8540) and 10 mM glucose (Sigma, Cat#G8769) for the Mitochondria Stress Tests. Cells were subsequently incubated at 37°C for 1 hour before being loaded into a Seahorse XFe24 Analyzer. Data analysis was performed using Wave (Agilent) software.

Flow cytometry

The live cell population was estimated using 10 μg/ml propidium iodide dye (Signa, Cat#P4170) and a BD LSRFortessa flow cytometer. Total cellular ROS was estimated using the DCFDA/H2DCFDA - Cellular ROS Assay Kit (Abcam Cat# ab113851) as per the manufacturer's instructions. Briefly, 2×10^5 cells were incubated with 20 μM of DCFDA dye for 30 minutes at 37°C. After incubation, cells were analyzed using a BD LSRFortessa flow cytometer. Mitochondria-specific reactive oxygen species (ROS) were estimated using MitoSOX Red (Molecular probes, Cat#M36008) as per the manufacturer's instructions. Briefly, 2×10^5 cells were incubated with 5 μM of MitoSoX Red dye for 10 minutes at 37°C. After incubation, cells were analyzed on a BD LSRFortessa flow cytometer.

The Mito-mKeima-based mitophagy assay was performed as per the published protocol (8). Briefly, pHAGE-mt-mKeima plasmid (a generous gift from Dr. Richard Youle) was transfected into WT or CBFB_KO MCF10A cells using Lipofectamine 3000 (Thermo Fisher, Cat# L3000001). After 24 hours, cells were harvested and analyzed using a

BD FACSymphony flow cytometer. Mito-mKeima, which localizes to the matrix of mitochondria, excites at 488 nm and 561 nm at pH 4 and pH 7, respectively. Therefore, excitation shifts from 561 nm to 488 nm in lysosomes. Emission was collected at 620 nm. Data analyses were performed using FlowJo.

ATP estimation

Total cellular ATP levels were measured using the Luminescent ATP Detection Assay Kit (Abcam, Cat# ab113849) as per the manufacturer's instructions.

Generation of stable cell lines

pBABE-puro-mCherry-EGFP-LC3B was a gift from Jayanta Debnath (Addgene plasmid # 22418; http://n2t.net/addgene:22418; RRID:Addgene_22418). pBabe-puro-HA-PIK3CA-H1047R plasmid was a gift from Jean Zhao (Addgene plasmid # 12524; http://n2t.net/addgene:12524; RRID:Addgene_12524). Retrovirus-based plasmids were packaged using Plat-A cells (Cell Biolabs, Cat# RV-102; RRID:CVCL_B489), and the supernatant containing retroviruses was collected at 48 and 72 hours post-transfection and combined. Cells were incubated with retrovirus supernatant and 6 μg/ml polybrene for transduction. After 24 hours, cells were replaced with fresh media containing selection antibiotics to generate stable cell lines.

Autophagic flux assay

Stable MCF10A cell lines carrying pBABE-puro-mCherry-EGFP-LC3B were established as described in the section of generation of stable cell lines. Cells were imaged using a Zeiss LSM 780 microscope with a 63X oil immersion objective lens, as described in the confocal section. mCherry and EGFP signals were analyzed on a BD LSRFortessa flow cytometer.

Genetic interaction analysis of mutations

Genetic interactions of the top 21 mutated genes in breast cancer were calculated as described previously(9). We calculated the genetic interactions between the top 21 mutations using the TCGA datasets. We used Fisher's exact test to report the genetic interactions with a p-value less than 0.05. Genetic interaction between two gene mutations with an odds ratio larger than one is considered co-occurring, while interaction with an odds ratio less than one indicates mutually exclusive. Oncoprints were generated using R.

Proteomic analysis of proteins encoded by the 21 mutated genes

Physical interactions of proteins encoded by the top 21 breast cancer mutated genes were extracted from a public dataset mapping the interactomes of breast cancer-related proteins (10). The dataset was a union of interactomes from three breast cell lines. Cytoscape was used to plot interactions.

Genetically engineered mouse models

All the mice were bred and maintained according to guidelines of the Institutional Animal Care and Use Committee (IACUC)-approved protocols of the National Cancer Institute (NCI). Breeder pairs of *Gt(ROSA)26Sor*^{tm1(Pik3ca*H1047R)Egan}/J (Stock No: 016977,

RRID:IMSR_JAX:016977), *Cbfb^tm2.1Ddg/J* (Stock No: 028550, RRID:IMSR_JAX:028550), and Tg(MMTV-Cre)4Mam/J (Stock No: 003553, RRID:IMSR_JAX:003553) strains were purchased from Jackson Laboratory. MMTV-Cre mice lines were genotyped using real time PCR [forward primer (FP): 5'-CCGGTTATTCAACTTGCACC-3' and reverse primer (RP) 5'-CTGCATTACCGGTCGATGCAAC- 3']. CBFB deletion was confirmed using real-time PCR with primers: FP: 5'-GCGCGCCAGTCACTTGTT-3' and RP: 5'- ATCCCACGAACCGAACCA-3'. *Pik3ca* mice were genotyped using primers; FP: 5'- AAAGTCGCTCTGAGTTGTTAT-3', RP1: 5'- GCGAAGAGTTTGTCCTCAACC -3' for mutant *Pik3ca* and RP2: 5'-GGAGCGGGAGAAATGGATATG -3' for wild type *Pik3ca*. All the mice for the cohort study were collected by crossing MMTV-Cre; Cbfb^fl/+Pik3ca^H1047R/+ genotypes of mice. All the animals in cohort were monitored regularly and euthanized as per the criteria in the approved animal study protocol (i.e., tumor reaches 2 cm in diameter or mice present severe health issues like breathing problems, inflammation, or loss of more than 15% of body weight). Harvested tumors were weighed, dissected into small pieces, and fixed in 10% neutral buffered formalin for 16 hours. Formalin-fixed tumors were embedded in paraffin blocks and stained with hematoxylin and eosin by Histoserv, Inc (Germantown, MD, USA). For RNAseq, RNA was extracted from freshly isolated tumors and quality-controlled by using the TapeStation (Agilent) to make sure that the RNA integrity number (RIN) was larger than 7. RNAseq was performed by the Next Generation Sequencing Core at the Center of Cancer Research, National Cancer Institute.

Clustering based on transcriptome

All analyses were carried out in NIH biowulf2 high-performance computing environment. We used the following R packages for the analyses: Seurat_3.1.4 and ComplexHeatmap_2.10.0. We have 18 mouse primary mammary tumors from a GEMM with Cbfb and Pik3ca mutations in the current study and 27 primary mouse tumors and lung metastasis from a previous study (a subset of GSE150928). Human breast cancer is well defined and can be classified into 5 subtypes: LumA, LumB, HER2, Basal, and Normal. We used 89 TCGA tumors, which were identified from LumA, LumB, HER2, and Basal subtypes that are the top 10% of samples closest to the centroid of each of the four subtypes. We used 39 genes of the PAM gene list that have homologs in both human and mouse reference genomes. To integrate mouse and human data, we used the IntegrateData function from the Seurat package to perform data harmonization and normalization across multiple datasets. The heatmap was generated with the ComplexHeatmap package.

Tumor xenografts and treatment

Studies were approved by the Institutional Animal Care and Use Committee (IACUC) of the National Cancer Institute (NCI), NIH. For CBFB_KO, PIK3CA(H1047R), or CBFB_KO+PIK3CA(H1047R) MCF10A xenografts, 2 million cells were resuspended in DMEM/F12 media supplemented with 25 mM HEPES (pH 7.4). The cell suspension was mixed with 25 μl Matrigel and was transplanted subcutaneously in NSG mice. For HCQ treatment, NSG mice transplanted with CBFB_KO MCF10A cells (transduced with pLenti6/ V5_luciferase) were randomized into control and treatment groups after consistent luciferase signal was detected using the IVIS® Spectrum *in vivo* imaging system (PerkinElmer). HCQ

was administered to the mice via intraperitoneal injection (IP) at 50 mg/kg in 0.1 ml sterile PBS once daily for 3 weeks. For single (HCQ or BYL719) and combinatorial (both HCQ and BYL719) treatments, NSG mice bearing palpable CBFB_KO+PIK3CA(H1047R) MCF10A xenografts were randomly separated into four groups based on tumor size, which were treated as follows: 1) vehicle group: sterile 0.1 ml PBS via IP plus 0.1 ml 0.5% (w/v) sterile methylcellulose via oral gavage, once daily for 3 weeks; 2) HCQ group: 50 mg/kg in 0.1 ml sterile PBS via IP, once daily for 3 weeks; 3) BYL719 group: 30 mg/kg in 0.1 ml sterile 0.5% (w/v) methylcellulose solution via oral gavage, daily for 3 weeks; 4) Combo group: the combination of 2) and 3). Mice were euthanized one day after the last treatment.

For single and combinatorial treatment of MCF7 xenografts and PDX (HCI-017, a kind gift of Dr. Alana Welm), 5 to 6-week-old (for MCF7) or 4-week-old (for the PDX) NSG mice were first implanted with 0.72 mg 60-day slow-release 17β-estradiol pellets (Innovative Research of America, Cat#:SE-121). Subsequently, 500,000 MCF7 cells were resuspended in 25 μl PBS and mixed with 25 μl Matrigel before being injected into the mammary fat pad; for the PDX, 4 mm X 2 mm fragments were transplanted into 3mm X 3mm pockets generated in the mammary fat pad. After palpable tumors were detected, NSG were randomized into four groups (vehicle, HCQ, BYL719, or combo), and the treatment schedule and dosing were the same as described above for MCF10A-derived xenografts.

Immunohistochemistry

FFPE slides were deparaffinized using xylene and serially hydrated using a decreasing percentage of alcohol (100% to 50%). Antigens were retrieved by sub-boiling temperature in 10 mM sodium citrate for 20 minutes (Ki-67) and 30 minutes (cCasp3). After cooling, endogenous peroxidases were inactivated by incubating in 3% H_2O_2 for 10 minutes. Subsequently, slides were washed with PBS containing 0.1% Tween 20 and blocked with goat serum. After blocking, slides were incubated overnight with primary antibodies at 4°C. The next day, slides were washed with PBS and incubated with a corresponding biotinylated secondary antibody (VECTASTAIN ABC kits, Cat# PK-4001 or BA-2000) for 30 minutes. Further, slides were incubated in biotin-avidin solution for 30 minutes at room temperature. The color was developed by incubating slides in DAB solution for 5-10 minutes.

Anchorage-independent growth assay

Anchorage-independent growth assays or soft agar colony assays were performed as described previously (4,9). Briefly, we first solidified a lower layer of 0.5 % agarose (Sea Kem LE Agarose, Cat# 50004) in a 6-well plate. Subsequently, we mixed 2,500 single cells with warm (37°C) 0.35% agarose in a culturing medium and quickly added the mixture on top of the 0.5% agarose lower layer. Colonies were counted and imaged with a 20X magnification on an Axiovert 25 microscope (Zeiss) at 15 and 30 days after plating. Transformation percentage was calculated by dividing the number of colonies formed by the total number of plated cells. The colony size was calculated based on images of twenty randomly selected colonies from duplicate wells. Three biological repeats were performed for each anchorage-independent growth assay.

Drug synergy study

Five thousand cells were plated in 96-well plates and treated with varying concentrations of drugs BYL719 and HCQ either alone or in combination (Combo) at various concentrations. At 72 hours after the treatment, cell viability was analyzed using a MTT-based (Cayman chemicals, Cat#21795) cell viability assay. IC_{50} values for each drug alone or in combination were computed using GraphPad and then used to calculate the Combination Index (CI) for estimating synergy (11). CI=(D)1/(Dx)1+(D)2/(Dx)2, where (Dx)1 and (Dx)2 are concentrations for drug 1 and drug 2, respectively, used alone to achieve a specific effect (50% killing in this study); (D)1 and (D)2 are concentrations for drug 1 and drug 2, respectively, to achieve the same effect. A CI of less than 1 indicates synergy. R synergyFinder library was used to calculate synergy scores with Bliss, HSA, and Loewe reference models for each combination treatment (12).

Statistical analyses

Genetic interaction analysis in breast cancer was analyzed using Fisher's exact test. Survival analysis of MMTV-Cre;Cbfb$^{fl/+}$;Pik3ca$^{H1047R/+}$ versus MMTV-Cre;Cbfb$^{+/+}$;Pik3ca$^{H1047R/+}$ genetically engineered mouse models (GEMM) were performed using GraphPad. RIP assay, soft agar colony assay and ATP estimation data were analyzed using the two-tailed t-test, assuming equal variance in the two groups. Tumor weight and tumor volume in xenograft assays were analyzed using the non-parametric Mann-Whitney test.

Data Availability

The RNAseq data in this study have been deposited into the Gene Expression Omnibus (GEO) database (Accession: GSE206598). Reagents including mouse strains generated from this study are available upon request.

Results

Integrated analyses of multiomics data to identify functional interactions of cancer genes in breast cancer

We hypothesized that a mutated gene pair with a genetic interaction (co-occurring or mutually exclusive) and physical interaction between their protein products plays a vital role in cancer progression. To test this hypothesis, we performed integrated analyses of genetic interactions of mutated genes in breast cancer and the proteomics interacting network of protein products encoded by these genes. Fisher's Exact Test was used to test pairwise genetic interaction of the top 21 mutated genes in the TCGA dataset (Fig. 1A). Among the 210 possible pairs, 20 were co-occurring and 10 were mutually exclusive (Supplementary Table 1), indicating that these gene pairs likely functionally interact in breast cancer.

We next utilized a public proteomics dataset that identifies the binding partners of proteins encoded by breast cancer-related genes (10). Among the 40 proteins analyzed in this dataset, 14 overlapped with the 21 genes used in our genetic interaction analyses (Fig. 1A and Supplementary Table 2). We filtered the list of all protein interactions to include only those involving the proteins encoded by the top 21 breast cancer genes and detected 67 non-redundant interactions (Fig. 1B and Supplementary Table 2). Among these protein pairs,

12 were also identified in our genetic interaction analyses (Fig. 1C). Although all these pairs may play a role in breast tumorigenesis, we chose to focus on PIK3CA-CBFB because the response rate to PIK3CA inhibitor, BYL719, needs further improvement. In addition, *CBFB* is highly mutated in breast, ovarian, prostate cancer, and acute myeloid leukemia; however, its functions in cancer remain largely unknown. Therefore, we reason that by studying the functional interaction between *PIK3CA* and *CBFB*, we may gain new insights that can be leveraged to enhance the efficacy of PIK3CA inhibitors and elucidate novel functions of CBFB in breast cancer.

Cooperation of CBFB LOF and mutant PIK3CA in human breast tumorigenesis

Previous studies have established that *CBFB* mutations in breast tumors are LOF (4) and *PIK3CA* mutations are oncogenic GOF (13). In both TCGA and METABRIC datasets, *CBFB* and *PIK3CA* mutations significantly co-occur (Fig. 1D). Thus, we hypothesized that CBFB LOF and mutant PIK3CA cooperate to promote breast tumor progression. To test this, we generated MCF10A cell lines expressing mutant PIK3CA (H1047R, a hotspot GOF mutation) or CBFB knockout (CBFB_KO) either alone or together in the same cell. CBFB_KO or PIK3CA (H1047R) alone transformed MCF10A cells as monitored by anchorage-independent growth assays (Supplementary Fig. 1A–B). However, MCF10A cells carrying both CBFB_KO and PIK3CA (H1047R) were significantly more effective in colony-forming than the other two lines. In a tumor formation assay, transplanted cells with both PIK3CA (H1047R) and CBFB_KO formed larger tumors and led to shorter survival of the mice than PIK3CA (H1047R) or CBFB_KO cells (Fig. 1E–G). Together, these data demonstrate that mutations in *PIK3CA* cooperate with CBFB loss to promote the transformation of human epithelial cells.

Cooperation of CBFB LOF and mutant PIK3CA in mouse mammary tumorigenesis

To test whether the functional interaction of CBFB LOF and mutant PIK3CA is conserved in mice, we generated genetically engineered mouse models (GEMMs) (Fig. 2A). We deleted the *Cbfb* gene in mammary epithelium using MMTV-driven Cre recombinase (hereinafter called the C model). Homozygous or heterozygous deletion of *Cbfb* did not induce the formation of mammary tumors even after a long median survival (>450 days) (Supplementary Fig. 2A). However, some mice developed lymphomas (Supplementary Fig. 2B). These results suggest that *Cbfb* deletion alone is insufficient to initiate mammary tumorigenesis. To express mutant Pik3ca in *Cbfb* deficient mice, we bred the C model with the *R26-Pik3ca^{H1047R}* transgenic mouse line, which carries a *Pik3ca^{H1047R}* allele downstream of a floxed STOP cassette in the ROSA26 (R26) locus (hereinafter called *Pik3ca^{H1047R}*). Mice homozygous for the *Pik3ca^{H1047R}* allele (*Pik3ca^{H1047R/H1047R}*) were born at a lower than predicted Mendelian ratio for unknown reasons; therefore, heterozygous mice (*Pik3ca^{H1047R/+}*) were used for subsequent studies. Most *MMTV-Cre;Cbfb^{fl/fl};Pik3ca^{H1047R/+}* mice developed severe inflammation around the eye and genital areas and had to be euthanized before palpable tumors formed, although a fraction of these mice developed small mammary tumors. Due to this complication, we focused on *MMTV-Cre;Cbfb^{fl/+};Pik3ca^{H1047R/+}* (hereinafter called the CP model) and *MMTV-Cre;Cbfb^{+/+};Pik3ca^{H1047R/+}* (hereinafter called the P model) mice.

Nulliparous CP and P mice had similar median survival: 258 and 285 days, respectively (p=0.32) (Supplementary Fig. 2C). Only 34% of P mice and 40% of CP mice developed mammary tumors (Supplementary Fig. 2D). In contrast, 100% of multiparous CP mice versus 25% multiparous P mice developed mammary tumors (Fig. 2B). Multiparous CP mice also had shorter median survival (182 days) and a higher tumor burden than multiparous P mice (Fig. 2C–D). Due to the high mammary tumor incidence in multiparous CP mice, we focused our studies on multiparous P and CP mice. Molecular profiling using the PAM50 signature showed that CP tumors mainly clustered with luminal-type A human breast tumors (Fig. 2E). In support of this, immunohistochemistry (IHC) indicated that CP tumors were estrogen receptor- (6.5-18.8%) and progesterone receptor-positive (1.0-2.8%), while P tumors were only estrogen receptor-positive (3.8-12.7%) (Fig. 2F). This observation is consistent with the TCGA data showing that *CBFB* mutations are enriched in hormone receptor-positive tumors (14). However, it is unknown whether tumors from the CP model are estrogen-dependent, which requires future investigation. Interestingly, MCF10A cells carrying CBFB_KO and PIK3CA(H1047R) expressed estrogen receptor alpha (ERα), as opposed to parental, CBFB_KO, or PIK3CA(H1047R) MCF10A cells (Supplementary Fig. 2E).

Histology analyses demonstrated that most P and CP tumors were adenosquamous carcinoma (Supplementary Fig. 2F). Genotyping analysis showed that CP tumors had a loss of heterozygosity (LOH) of the *Cbfb* gene (Supplementary Fig. 2G), which also occurs in human breast tumors (Supplementary Fig. 2H). Thus, we have developed a GEMM (the CP model) that recapitulates the cooperation of CBFB deficiency and mutant PIK3CA in human breast tumors.

CBFB and its binding partner, hnRNPK, localize to mitochondria and bind to mitochondrially encoded mRNA

We next investigated the functional interaction between CBFB and PIK3CA in breast tumors and focused primarily on CBFB, as its role in breast cancer is relatively unknown. CBFB has been described as a transcription cofactor for RUNX proteins (15). However, we recently identified both nuclear and cytoplasmic functions for CBFB in breast cancer cells and found that RUNX1 plays a crucial role in maintaining the nuclear levels of CBFB (4,9). In the cytoplasm, CBFB binds to hundreds of mRNAs through its RNA-binding partner hnRNPK (4). RUNX1 shuttles CBFB into the nucleus, where these two proteins form a transcriptional complex to regulate gene expression (4,9). To identify the main downstream pathway(s) regulated by CBFB, we subjected CBFB-bound mRNAs (Supplementary Table 3) to IPA (Ingenuity Pathway Analysis). The top enriched pathways were Wnt/beta-catenin signaling, mitochondrial dysfunction, RAR (retinoic acid receptor) activation, oxidative phosphorylation, and aryl hydrocarbon receptor signaling (Fig. 3A, top). We chose to study the function of CBFB in mitochondria for two reasons. First, CBFB and hnRNPK bound to the majority of mitochondrially encoded mRNAs (mt-mRNAs) (Fig. 3A, bottom, and Fig. 3B). Second, we performed a Gene Ontology analysis of CBFB and hnRNPK-bound mRNAs. Among the top 10 enriched GO terms, six were related to adenosine triphosphate (ATP) generation, a major function of mitochondria (Supplementary Table 3).

To validate the binding of mt-mRNAs to CBFB and hnRNPK, we used RNA immunoprecipitation (RIP) followed by real-time PCR. Most (12 out of 13) mt-mRNAs were enriched in the CBFB pull-down (Supplementary Fig. 3A). Importantly, the association was not detected in CBFB knockout (KO) MCF10A cells, indicating the CBFB antibody is specific. In addition, CBFB depletion reduced the binding of hnRNPK with mt-mRNAs (Supplementary Fig. 3B). Exogenous expression of CBFB in MCF7 cells, a breast cancer cell line that endogenously expresses less CBFB than MCF10A cells (Supplementary Fig. 3C), enhanced the binding of hnRNPK to mt-mRNAs (Supplementary Fig. 3D). In addition, we observed similar results in BT474 cells (Supplementary Fig. 3E). Furthermore, knockdown of CBFB in MDA-MBA-361 cells (Supplementary Fig. 3F) decreased the binding of hnRNPK to mt-mRNAs (Supplementary Fig. 3G). Together, these data confirm the binding of CBFB and hnRNPK to mt-mRNAs in human breast cells.

Binding to mt-mRNAs suggests that CBFB and hnRNPK localize to mitochondria because mt-mRNAs are found in the mitochondrial matrix. Consistent with this possibility, both CBFB and hnRNPK co-localized with the mitochondrial marker COX IV in MCF10A cells (Fig. 3C–D). In addition, cell fractionation followed by immunoblotting detected both CBFB and hnRNPK in the mitochondrial fraction (Fig. 3E), and immunoprecipitation verified their interaction in this fraction (Fig. 3F). Thus, CBFB and hnRNPK localize to and interact in mitochondria.

CBFB has no RNA binding domain and relies on hnRNPK to interact with RNAs (4). To corroborate the direct binding of hnRNPK to mt-mRNAs, we re-analyzed a public hnRNPK eCLIP dataset from the ENCODE project (16), which maps RNA binding sites of hnRNPK in K562 cells, a myelogenous leukemia cell line. This independent dataset showed that hnRNPK directly binds to mt-mRNAs (Fig. 3G), and the hnRNPK binding sites within these mt-mRNAs contained poly-cytosine (poly-C) tracts, the known motif for hnRNPK (4). This analysis suggests that CBFB binds to mt-mRNAs through hnRNPK.

CBFB moonlights as a regulator of mitochondrial translation

To search for the putative function of CBFB in mitochondria, we performed BioID (proximity-dependent biotin identification) to identify proteins that are in close proximity to and likely to interact with CBFB in cells (17). These proteins are referred to as the "CBFB interactome" hereinafter. We identified 838 proteins (enrichment > 2-fold) in the CBFB interactome (Fig. 4A and Supplementary Table 4). Among them, 39 likely localize to mitochondria based on MitoCarta 3.0 (18) (Fig. 4B). Hypergeometric distribution showed that the overlap of the CBFB interactome and MitoCarta 3.0 is not random (p=0.017), supporting the notion that CBFB plays a functional role in mitochondria. Two proteins are likely involved in the mitochondrial translocation of CBFB: TIMM50, a subunit of the TIM23 translocase complex localized to the mitochondrial inner membrane, and TOMM40, a subunit of the translocase in the mitochondrial outer membrane. Additionally, TUFM (also called mtEF-Tu) and several mitoribosome subunits, MRPS11, MRPS28, and MRPS5, were identified.

TUFM is an essential elongation factor in mitochondrial translation (19). Therefore, we first verified the interaction between CBFB and TUFM. In addition to BioID followed

by immunoblotting (Fig. 4C), we were able to co-immunoprecipitate CBFB and TUFM (Fig. 4D). We also performed proximity ligation assay (PLA) in MCF10A cells (Fig. 4E–F) and four *in vivo* models: KRAS-driven (Supplementary Fig. 4A) and PIK3CA(H1047)-driven MCF10A xenografts models (Supplementary Fig. 4B), normal human breast tissue (Supplementary Fig. 4C), and GEMMs (Supplementary Fig. 4D). There was no difference in PIK3CA expression in P and CP tumors, while CBFB expression was very low in CP tumors (Supplementary Fig. 4E). In all these experiments, we detected the interaction between CBFB and TUFM, indicating that this interaction occurs in multiple cell contexts.

The interaction between CBFB and TUFM suggests that CBFB regulates mitochondrial translation. To test this possibility, we applied a newly developed *in situ* imaging method to measure mitochondrial translation (6,20). Using this approach, we observed that mitochondrial translation was reduced about 3-fold in CBFB_KO MCF10A cells as compared to WT (Fig. 4G–H). This result was verified by in-gel fluorescence imaging (Fig. 4I). Because this *in situ* imaging assay cannot be performed *in vivo*, we used the correlation between CBFB and mt-proteins (assessed by IHC) as a proxy for mitochondrial translation regulation by CBFB. Among the several mt-protein antibodies tested, only MT-CO1 antibody performed well in IHC. In P and CP tumors, we observed a strong correlation between CBFB and MT-CO1 protein levels (Fig. 4J and Supplementary Fig. 4F).

The steady-state levels of several mitochondrially encoded proteins (mt-proteins) were also lower in CBFB_KO cells than in WT cells (Fig. 4K). In contrast, other mitochondrially localized proteins (COX IV, HSP60, and Cytochrome C), whose mRNAs were not bound by CBFB and hnRNPK, had comparable levels between CBFB KO and WT cells. The specificity for CBFB- and hnRNPK-bound targets led us to hypothesize that CBFB regulates mitochondrial translation by modulating the binding of TUFM to mt-mRNAs. Indeed, RIP showed that CBFB depletion reduced the binding of TUFM to mt-mRNAs (Fig. 4L). The reduced binding of TUFM to mt-mRNAs was not due to the change of TUFM protein levels (Supplementary Fig. 4G). Similarly, P and CP tumors displayed no difference in TUFM expression (Supplementary Fig. 4H). Given its role in translating almost the whole mitochondrial genome, CBFB also functions as a direct regulator of mitochondrial translation.

We next examined whether mitochondrial translation is dysregulated in breast cancer cells. MCF7 and BT474 cells endogenously express lower levels of CBFB than MCF10A cells (4,9). Therefore, we overexpressed CBFB in these two cell lines and found that the overexpression (OE) increased the steady-state levels of mt-proteins (Supplementary Fig. 4I), suggesting that mitochondrial translation is downregulated in these breast cancer cells. Indeed, *in situ* imaging of mitochondrial translation showed that CBFB_OE enhanced mitochondrial translation in MCF7 cells (Fig. 4M and Supplementary Fig. 4J). These results suggest that dysregulation of CBFB-regulated mitochondrial translation is reversible in breast cancer cells.

Mitochondrial translation dysregulation causes mitochondrial defects and metabolic reprogramming

All mt-proteins are essential subunits of the five complexes in the electron transport chain (ETC). Thus, we reasoned that mitochondrial translation defects would cause disruption of the ETC and loss of mitochondrial membrane potential. To test this, we stained WT and CBFB_KO MCF10A cells with MitoTracker Green and MitoTracker Red, which both stain mitochondria but are membrane potential independent or dependent, respectively (Fig. 5A). While we did not observe an obvious difference in the MitoTracker Green signal in WT and CBFB_KO MCF10A cells, the MitoTracker Red signal was greatly reduced in CBFB_KO cells (Fig. 5A–B), suggesting that mitochondrial translation downregulation promotes the loss of mitochondrial membrane potential.

We next examined the relationship between mitochondrial translation and mitochondrial fitness using the Seahorse Cell Mito Stress Test. Interestingly, CBFB_KO cells had higher oxygen consumption, elevated basal respiration, and reduced spare respiration capacity than WT cells (Fig. 5C–D), potentially due to proton leak caused by ETC defects. Consistent with this, CBFB_KO cells had less ATP than WT cells (Fig. 5E), suggesting a decoupling of oxygen consumption and energy generation. In addition, ROS levels in the whole cell (DCFDA) and mitochondria (MitoSOX) were higher in CBFB_KO cells than WT cells (Fig. 5F), indicating that mitochondria in CBFB_KO cells are defective, diverting oxygen from ATP generation to ROS. Mitochondrial fission also occurs as a consequence of mitochondrial damage and facilitates mitophagy-mediated quality control (21). Using super-resolution microscopy and 3-D reconstruction, we observed that mitochondria in CBFB_KO cells had a higher degree of fission than WT cells (Fig. 5G), further supporting the notion that CBFB deficiency causes mitochondrial defects.

We hypothesized that CBFB_KO cells utilize aerobic glycolysis as a compensatory energy generation mechanism due to their defective oxidative phosphorylation. To test this, we performed the Seahorse Glycolysis Stress Test. Indeed, we observed that the CBFB_KO cells had higher glycolysis, glycolytic capacity, and glycolytic reserve (Fig. 5H–I). Thus, defective mitochondrial translation is associated with metabolic reprogramming, including the Warburg effect.

Mitochondrial translation defects lead to elevated autophagy/mitophagy and render cells sensitive to autophagy inhibition

Autophagy often occurs in response to metabolic stress. Given the profound metabolic changes caused by mitochondrial translation dysregulation, we tested whether autophagy is altered in CBFB_KO cells using an autophagy flux assay (22). We stably transduced WT and CBFB_KO MCF10A cells with LC3B fused to tandem mCherry and enhanced GFP (EGFP) fluorescent proteins. Because the EGFP, but not the mCherry, signal is suppressed by an acidic environment, cells with elevated autophagy have a lower EGFP signal than cells with normal autophagy, which have a balanced mCherry-to-EGFP ratio. CBFB_KO cells had a similar mCherry signal but a lower EGFP signal than WT cells (Fig. 6A and Supplementary Fig. 5A), suggesting that CBFB_KO cells had enhanced autophagy. In addition, the mCherry signal was more punctate in CBFB_KO cells than in WT cells,

indicating that most mCherry-EGFP-LC3B in CBFB_KO cells formed autolysosomes (Fig. 6A). Consistent with the autophagy influx assay, immunoblotting showed that LC3-I and LC3-II (lipidated form of LC3) levels were higher in CBFB_KO cells (Fig. 6B). Futher, the LC3 signal was higher in CP tumors than in P tumors (Fig. 6C), suggesting that the elevated autophagy upon CBFB deletion also occurs in breast tumor *in vivo*.

We next examined the molecular mechanisms underlying enhanced autophagy. One of the initial steps in autophagy is ULK1 (Unc-51 like autophagy activating kinase 1) phosphorylation (23). Ulk1 phosphorylation at serine 555 (phos-S555) by AMPK (adenosine monophosphate-activated protein kinase) promotes autophagy, while phosphorylation of serine 757 (phos-S757) by mTOR (the mammalian target of rapamycin) inhibits autophagy (23,24). We reasoned that the lower levels of ATP in CBFB_KO cells (Fig. 6D) would activate AMPK, thus promoting subsequent ULK1 phos-S555 and autophagy. Using immunoblotting, we observed that AMPK phos-T172 levels were higher in CBFB_KO cells than in WT cells (Fig. 6D), suggesting higher AMPK activation in CBFB_KO cells. In addition, ULK1 phos-S555 levels were higher in CBFB_KO cells than in WT cells, while ULK1 phos-S757 levels were lower (Fig. 6D). These results suggest that mitochondrial translation dysregulation enhances autophagy via the AMPK-ULK1 axis.

ULK1 phos-S555 is also required for mitophagy, a type of autophagy to remove damaged mitochondria to promote survival (25). Therefore, we examined whether mitophagy is upregulated in CBFB_KO cells by performing co-staining of COX IV, a mitochondrial marker, and LAMP1, a lysosomal marker. The proportion of mitochondria co-localized with lysosomes was higher in CBFB_KO cells than in WT cells (Fig. 6E and Supplementary Fig. 5B). Single-cell analysis using machine learning gave a similar result (Fig. 6F and Supplementary Fig. 5C). To further examine mitophagy, we used two independent approaches: a quantitative flow cytometry-based mitophagy assay, mito-mKeima (8), and electron microscopy. Both methods showed that mitophagy was higher in CBFB_KO cells than WT cells (Fig. 6G and Supplementary Fig. 5D). Together, these data indicate that CBFB deficiency-induced mitochondrial translation defects are associated with elevated mitophagy.

Since a primary function of autophagy/mitophagy is to promote cell survival upon metabolic stress throughout tumor progression, we tested the effect of autophagy inhibition on the survival of WT and CBFB_KO MCF10A cells *in vitro* and tumor growth *in vivo*. Using hydroxychloroquine (HCQ), a general autophagy inhibitor, we observed that autophagy inhibition increased cell death of CBFB_KO cells, but not WT cells, *in vitro* (Supplementary Fig. 5E). In addition, CBFB_KO MCF10A cells form tumors in immunocompromised NSG (NOD-scid, IL2R gamma[null]) mice (4). Therefore, we tested the effect of HCQ on tumor growth and found it decreased the growth of CBFB_KO xenografts (Fig. 6H–I and Supplementary Fig. 5F). These results indicate that cells with defective CBFB-regulated mitochondrial translation become dependent on autophagy/mitophagy for survival. This autophagy dependence for survival provides an opportunity for therapeutic targeting.

Mutant PIK3CA does not alter the function of CBFB in mitochondrial translation

The PI3K signaling pathway also regulates cancer cell metabolism (26). Therefore, we tested whether the PIK3CA (H1047R) mutant modulates the role of CBFB in mitochondrial translation. Using the *in situ* mitochondrial translation assay, we found that PIK3CA (H1074R) did not alter CBFB-regulated mitochondrial translation in MCF10A cells (Supplementary Fig. 6A–B). Next, we tested whether PIK3CA (H1047R) affects mitochondrial respiration and glycolysis. PIK3CA (H1047R) overexpression alone did not affect mitochondrial respiration and did not alter the mitochondrial stress observed for CBFB_KO cells (Supplementary Fig. 6C). Of note, PIK3CA (H1047R) boosted glycolysis similarly to CBFB deletion (Supplementary Fig. 6D), which is consistent with the classical role of PI3K signaling in enhancing glucose uptake (26). However, it did not further increase glycolysis in CBFB_KO cells. In addition, PIK3CA (H1047R) did not alter CBFB deficiency-induced autophagy (Supplementary Fig. 6E). Similarly, CBFB had no effect on PIK3CA (H1047R) activity, as indicated by phospho-AKT levels (Supplementary Fig. 6E). Furthermore, IHC analyses showed MCF10A xenografts driven by CBFB KO and by both CBFB KO and PIK3CA (H1047R) overexpression had similar levels of downregulation of MT-CO1 and upregulation of autophagy (Supplementary Fig. 6F). Together, these results indicate that mutant PIK3CA does not modulate the CBFB-mitochondrial translation-autophagy axis.

Autophagy and PIK3CA inhibitors synergistically kill breast cancer cells *in vitro*

Because mitochondrial translation dysregulation renders breast tumor cells addicted to autophagy for survival (Fig. 6H–I and Supplementary Fig. 5D–E), we investigated whether we could exploit this vulnerability to develop new therapeutic strategies for breast cancer. We first tested whether PIK3CA (H1047R) alters the dependence of CBFB_KO MCF10A cells on autophagy for survival *in vitro*. HCQ treatment for 24 hours increased cleaved caspase 3 (cCasp3) levels in CBFB_KO, but not WT, MCF10A cells (Fig. 7A). When PIK3CA (H1047R) was present, the treatment induced higher levels of cCasp3 (Fig. 7A). We then tested another two autophagy inhibitors, MRT68921 (ULK1/2 inhibitor) and SBI-0206965 (ULK1 inhibitor). Similar to HCQ, both inhibitors induced apoptosis, further enhanced by PIK3CA (H1047R) (Supplementary Fig. 7A–B). These results suggest that the presence of mutant PIK3CA increases the dependency of CBFB-deficient cells on autophagy for survival, therefore providing a rationale for combining autophagy and PIK3CA inhibitors.

We next assessed the efficacy of autophagy and PIK3CA inhibitor combination treatment on breast cancer cell killing. HCQ was used as the autophagy inhibitor in our combination studies because it is an FDA-approved drug for malaria and its safety profile is well-documented. For inhibiting PIK3CA, we used BYL719 (PIQRAY or Alpelisib), a recent FDA-approved first-in-class PIK3CA-specific inhibitor for treating breast cancer. HCQ and BYL719 had a synergistic killing effect in both MCF7 cells, which express low levels of CBFB and carry a PIK3CA mutation, and CBFB_KO MCF10A cells expressing PIK3CA (H1047R) based on several algorithms to calculate synergy: the Combination Index (CI) approach (11), Bliss, HSA (Highest single agent), and Loewe (12) (Fig. 7B–C and

Supplementary Fig. 8A–B). Therefore, these two drugs can synergistically kill breast cancer cells *in vitro*.

Autophagy and PIK3CA inhibitors synergistically inhibit tumor growth

To examine the effect of combination autophagy and PIK3CA inhibition on breast tumor growth, we treated mice bearing MCF7 xenografts with HCQ and BYL719 as single agents or in combination (Fig. 7D). While HCQ and BYL719 each decreased tumor growth, the combination further reduced tumor growth compared to the single-agent treatments (Fig. 7E–G). The synergy was also observed for xenografts derived from CBFB_KO MCF10A cells expressing mutant PIK3CA (H1047), though only HCQ decreased tumor growth as a single agent (Supplementary Fig. 9A–D). To gain insights into the mechanisms underlying the synergistic killing effect of HCQ and BYL719 *in vivo*, we performed immunohistochemistry (IHC) to assess cCasp3 and Ki-67 expression in tumor tissues. HCQ mainly increased apoptosis (cCasp3), while BYL719 reduced the proliferation (Ki-67) of MCF7 tumors *in vivo* (Fig. 7H–K). These results suggest that combining autophagy and PIK3CA inhibitors is a promising therapeutic strategy for treating breast tumors with mitochondrial translation defects.

To test the synergistic effect of HCQ and BYL719 in a more clinically relevant setting, we turned to a patient-derived xenograft (PDX) model of breast cancer. In a collection of breast cancer PDXs, we identified one PDX (HCI-017) that carried both CBFB and PIK3CA mutations (27). Using this PDX, we observed the synergistic effect of HCQ and BYL719 on inhibiting tumor growth (Fig. 7I–O), and one mouse was tumor-free after the combo treatment (Fig. 7N). Therefore, in both cell line-derived xenografts and a PDX model, autophagy and PIK3CA inhibitors synergistically impair tumor growth.

Discussion

Mitochondrial translation defects and the Warburg effect

Here we show that CBFB-regulated mitochondrial translation is an unappreciated regulatory step in breast cancer metabolism that synergizes with mutant PIK3CA in breast cancer progression. This finding sheds new light on a long-standing debate related to the Warburg theory: whether cancer cells rely on aerobic glycolysis rather than mitochondrial respiration due to dysfunctional mitochondria. Although Dr. Warburg postulated that cancer cells have defective mitochondria, prior studies searching for mitochondrial defects in cancer cells have been largely unsuccessful (28–30). Our results provide evidence that mitochondrial defects underpin cancer cell reliance on aerobic glycolysis in a subset of breast cancer cells, such as those carrying *CBFB* mutations. Other mechanisms can also drive the Warburg effect (30), such as increased glucose uptake in *PIK3CA* mutant cancer cells (26). However, unlike CBFB deficiency, *PIK3CA* mutations increase glycolysis without detectable changes in mitochondrial translation and function. Therefore, the mechanism driving the Warburg effect can vary depending on the cellular and mutational context.

In addition to breast cancer, the *CBFB* gene is altered in other cancers, including 4% prostate, 9% ovarian, and 5% acute myeloid leukemias. Therefore, it will be interesting

to study whether CBFB deficiency-induced mitochondrial defects also cause the Warburg effect in these cancer types. In addition to mutation, CBFB is downregulated by other unknown mechanisms in ER-positive breast cancer cells (4). For example, despite carrying a WT *CBFB* gene, MCF7 and BT474 cells express lower levels of CBFB protein than non-tumorigenic MCF10A cells (4). Therefore, the prevalence of mitochondrial translation defects may be underestimated if based only on the mutational status of *CBFB*.

The unexpected role of CBFB in mitochondrial translation

We found that CBFB regulates 12 out of 13 mitochondrially encoded proteins, which are essential building blocks of the ETC, and functions as a master regulator of mitochondrial translation. CBFB was first reported as a non-DNA binding transcriptional cofactor for the RUNX family proteins (31). Several transcription-independent roles of CBFB were later described, including HIV infection and cytoplasmic translation (4,32). Since cytoplasmic translation and mitochondrial translation consist of two distinct sets of machinery, this study reveals a new role of CBFB in mitochondrial function. Interestingly, although several independent approaches (immunofluorescence, cell fractionation, RIP-seq, BioID, and PLA) indicated that CBFB localizes to mitochondria, CBFB does not contain a predicted mitochondrial targeting sequence (MTS). Recently, it has been shown that many known mitochondrial proteins lack a conventional MTS and use a non-canonical MTS for mitochondrial translocation (33). Therefore, it is possible that CBFB uses a non-canonical MTS for mitochondrial localization.

In yeast, cytoplasmic translation and mitochondrial translation are synchronized to ensure energetic homeostasis (34), and this is likely conserved in mammalian cells. However, the factor(s) involved in this coordination has been elusive. Our results suggest that CBFB coordinates the translation of a fraction of cytoplasmic mRNAs (cyto-mRNAs) and mt-mRNAs. Since CBFB and hRNPK only regulate the translation of a fraction (about 1,000) of cyto-mRNAs (4), other coordinating factors of these two processes may exist. Our prior studies suggest that the preferential binding of hnRNPK to RNAs containing C-tracts may play an essential role in mRNA selection (4). Of note, 12 of the 13 mt-mRNAs have C-tracts, as they are encoded by the G-rich heavy strand of mt-DNA (Fig. 3F, eCLIP). Therefore, it is possible that mammalian cells utilize the C-tract binding preference of hnRNPK to regulate mitochondrial translation.

Enhanced autophagy/mitophagy is a vulnerability in cancer cells with mitochondrial translation defects

Our study establishes a connection between mitochondrial translation defects and autophagy dependence for survival. Autophagy has been challenging to target as a cancer treatment because of its context-dependent role in tumor growth; autophagy appears to be inhibitory at the early stages of tumorigenesis but promotes tumor progression at later stages (35). In addition, genetic makeup also modulates autophagy dependence and sensitivity to autophagy inhibition, as shown for mouse pancreatic cancers of varying p53 status (36). There is, however, a resurgent interest in autophagy inhibition for cancer treatment (37). In our study, the metabolic stress caused by mitochondrial translation defects renders breast cancer cells dependent on autophagy for survival. Thus, *CBFB* mutation status may be a useful

biomarker for autophagy dependence, which can be used to select patients likely to respond to autophagy inhibition(38).

Monotherapy with autophagy inhibitors has been largely ineffective (38), potentially due to the plasticity of cancer metabolism. Several case reports have documented success upon combining autophagy inhibitors with other targeted therapies (39,40). In the current study, we found that the combination of FDA-approved inhibitors of autophagy (HCQ) and PIK3CA (BYL719) was a promising therapeutic strategy for treating breast tumors with mitochondrial translation defects. One possibility for the synergy is that HCQ effectively targets slowly proliferating breast cancer cells, as we have previously shown that HCQ can kill dormant breast tumor cells (41). In the current study, BYL719 blocks proliferation in the MCF7 xenograft model (Fig. 7K). Therefore, BYL719 may induce cell dormancy, facilitating subsequent elimination by HCQ. Another possibility is that BYL719 and HCQ target separate dormant and proliferative populations in a tumor to achieve synergy. Regardless of the mechanism of synergy, our findings identify a promising avenue for future clinical exploration and define CBFB status as a potential biomarker for sensitivity to autophagy inhibition.

Supplementary Material

Refer to Web version on PubMed Central for supplementary material.

Acknowledgements

References

1. Andre F, Ciruelos E, Rubovszky G, Campone M, Loibl S, Rugo HS, et al. Alpelisib for PIK3CA-Mutated, Hormone Receptor-Positive Advanced Breast Cancer. N Engl J Med 2019;380:1929–40 [PubMed: 31091374]

2. Jaaks P, Coker EA, Vis DJ, Edwards O, Carpenter EF, Leto SM, et al. Effective drug combinations in breast, colon and pancreatic cancer cells. Nature 2022;603:166–73 [PubMed: 35197630]

3. Li M, Gou H, Tripathi BK, Huang J, Jiang S, Dubois W, et al. An Apela RNA-Containing Negative Feedback Loop Regulates p53-Mediated Apoptosis in Embryonic Stem Cells. Cell Stem Cell 2015;16:669–83 [PubMed: 25936916]

4. Malik N, Yan H, Moshkovich N, Palangat M, Yang H, Sanchez V, et al. The transcription factor CBFB suppresses breast cancer through orchestrating translation and transcription. Nat Commun 2019;10:2071 [PubMed: 31061501]

5. van der Walt S, Schonberger JL, Nunez-Iglesias J, Boulogne F, Warner JD, Yager N, et al. scikit-image: image processing in Python. PeerJ 2014;2:e453 [PubMed: 25024921]

6. Yousefi R, Fornasiero EF, Cyganek L, Montoya J, Jakobs S, Rizzoli SO, et al. Monitoring mitochondrial translation in living cells. EMBO Rep 2021;22:e51635 [PubMed: 33586863]

7. Yan H, Malik N, Kim YI, He Y, Li M, Dubois W, et al. Fatty acid oxidation is required for embryonic stem cell survival during metabolic stress. EMBO Rep 2021;22:e52122 [PubMed: 33950553]

8. Wang C. A Sensitive and Quantitative mKeima Assay for Mitophagy via FACS. Curr Protoc Cell Biol 2020;86:e99 [PubMed: 31876372]

9. Malik N, Yan H, Yang HH, Ayaz G, DuBois W, Tseng YC, et al. CBFB cooperates with p53 to maintain TAp73 expression and suppress breast cancer. PLoS Genet 2021;17:e1009553 [PubMed: 33945523]

10. Kim M, Park J, Bouhaddou M, Kim K, Rojc A, Modak M, et al. A protein interaction landscape of breast cancer. Science 2021;374:eabf3066 [PubMed: 34591612]

11. Chou TC, Talalay P. Quantitative analysis of dose-effect relationships: the combined effects of multiple drugs or enzyme inhibitors. Adv Enzyme Regul 1984;22:27–55 [PubMed: 6382953]

12. Yadav B, Wennerberg K, Aittokallio T, Tang J. Searching for Drug Synergy in Complex Dose-Response Landscapes Using an Interaction Potency Model. Comput Struct Biotechnol J 2015;13:504–13 [PubMed: 26949479]

13. Isakoff SJ, Engelman JA, Irie HY, Luo J, Brachmann SM, Pearline RV, et al. Breast cancer-associated PIK3CA mutations are oncogenic in mammary epithelial cells. Cancer Res 2005;65:10992–1000 [PubMed: 16322248]

14. Banerji S, Cibulskis K, Rangel-Escareno C, Brown KK, Carter SL, Frederick AM, et al. Sequence analysis of mutations and translocations across breast cancer subtypes. Nature 2012;486:405–9 [PubMed: 22722202]

15. Ito Y, Bae SC, Chuang LS. The RUNX family: developmental regulators in cancer. Nat Rev Cancer 2015;15:81–95 [PubMed: 25592647]

16. Consortium EP. An integrated encyclopedia of DNA elements in the human genome. Nature 2012;489:57–74 [PubMed: 22955616]

17. Roux KJ, Kim DI, Burke B. BioID: a screen for protein-protein interactions. Curr Protoc Protein Sci 2013;74:19 23 1–19 23 14

18. Rath S, Sharma R, Gupta R, Ast T, Chan C, Durham TJ, et al. MitoCarta3.0: an updated mitochondrial proteome now with sub-organelle localization and pathway annotations. Nucleic Acids Res 2021;49:D1541–7 [PubMed: 33174596]

19. Ott M, Amunts A, Brown A. Organization and Regulation of Mitochondrial Protein Synthesis. Annu Rev Biochem 2016;85:77–101 [PubMed: 26789594]

20. Lisci M, Barton PR, Randzavola LO, Ma CY, Marchingo JM, Cantrell DA, et al. Mitochondrial translation is required for sustained killing by cytotoxic T cells. Science 2021;374:eabe9977 [PubMed: 34648346]

21. Youle RJ, van der Bliek AM. Mitochondrial fission, fusion, and stress. Science 2012;337:1062–5 [PubMed: 22936770]

22. N'Diaye EN, Kajihara KK, Hsieh I, Morisaki H, Debnath J, Brown EJ. PLIC proteins or ubiquilins regulate autophagy-dependent cell survival during nutrient starvation. EMBO Rep 2009;10:173–9 [PubMed: 19148225]

23. Egan DF, Shackelford DB, Mihaylova MM, Gelino S, Kohnz RA, Mair W, et al. Phosphorylation of ULK1 (hATG1) by AMP-activated protein kinase connects energy sensing to mitophagy. Science 2011;331:456–61 [PubMed: 21205641]

24. Kim J, Kundu M, Viollet B, Guan KL. AMPK and mTOR regulate autophagy through direct phosphorylation of Ulk1. Nat Cell Biol 2011;13:132–41 [PubMed: 21258367]

25. Palikaras K, Lionaki E, Tavernarakis N. Mechanisms of mitophagy in cellular homeostasis, physiology and pathology. Nat Cell Biol 2018;20:1013–22 [PubMed: 30154567]

26. Hopkins BD, Goncalves MD, Cantley LC. Insulin-PI3K signalling: an evolutionarily insulated metabolic driver of cancer. Nat Rev Endocrinol 2020;16:276–83 [PubMed: 32127696]

27. Guillen KP, Fujita M, Butterfield AJ, Scherer SD, Bailey MH, Chu Z, et al. A human breast cancer-derived xenograft and organoid platform for drug discovery and precision oncology. Nat Cancer 2022;3:232–50 [PubMed: 35221336]

28. Potter M, Newport E, Morten KJ. The Warburg effect: 80 years on. Biochem Soc Trans 2016;44:1499–505 [PubMed: 27911732]

29. Wallace DC. Mitochondria and cancer. Nat Rev Cancer 2012;12:685–98 [PubMed: 23001348]

30. Liberti MV, Locasale JW. The Warburg Effect: How Does it Benefit Cancer Cells? Trends Biochem Sci 2016;41:211–8 [PubMed: 26778478]

31. Wang S, Wang Q, Crute BE, Melnikova IN, Keller SR, Speck NA. Cloning and characterization of subunits of the T-cell receptor and murine leukemia virus enhancer core-binding factor. Mol Cell Biol 1993;13:3324–39 [PubMed: 8497254]

32. Jager S, Kim DY, Hultquist JF, Shindo K, LaRue RS, Kwon E, et al. Vif hijacks CBF-beta to degrade APOBEC3G and promote HIV-1 infection. Nature 2011;481:371–5 [PubMed: 22190037]

33. Bykov YS, Flohr T, Boos F, Zung N, Herrmann JM, Schuldiner M. Widespread use of unconventional targeting signals in mitochondrial ribosome proteins. EMBO J 2022;41:e109519 [PubMed: 34786732]

34. Couvillion MT, Soto IC, Shipkovenska G, Churchman LS. Synchronized mitochondrial and cytosolic translation programs. Nature 2016;533:499–503 [PubMed: 27225121]

35. Mathew R, Karantza-Wadsworth V, White E. Role of autophagy in cancer. Nat Rev Cancer 2007;7:961–7 [PubMed: 17972889]

36. Rosenfeldt MT, O'Prey J, Morton JP, Nixon C, MacKay G, Mrowinska A, et al. p53 status determines the role of autophagy in pancreatic tumour development. Nature 2013;504:296–300 [PubMed: 24305049]

37. Dolgin E. Anticancer autophagy inhibitors attract 'resurgent' interest. Nat Rev Drug Discov 2019;18:408–10 [PubMed: 31160763]

38. Levy JMM, Towers CG, Thorburn A. Targeting autophagy in cancer. Nat Rev Cancer 2017;17:528–42 [PubMed: 28751651]

39. Kinsey CG, Camolotto SA, Boespflug AM, Guillen KP, Foth M, Truong A, et al. Protective autophagy elicited by RAF-->MEK-->ERK inhibition suggests a treatment strategy for RAS-driven cancers. Nat Med 2019;25:620–7 [PubMed: 30833748]

40. Bryant KL, Stalnecker CA, Zeitouni D, Klomp JE, Peng S, Tikunov AP, et al. Combination of ERK and autophagy inhibition as a treatment approach for pancreatic cancer. Nat Med 2019;25:628–40 [PubMed: 30833752]

41. Vera-Ramirez L, Vodnala SK, Nini R, Hunter KW, Green JE. Autophagy promotes the survival of dormant breast cancer cells and metastatic tumour recurrence. Nature Communications 2018;9:1944

Significance:

CBFB-regulated mitochondrial translation is a regulatory step in breast cancer metabolism and synergizes with mutant PI3K in breast cancer progression.
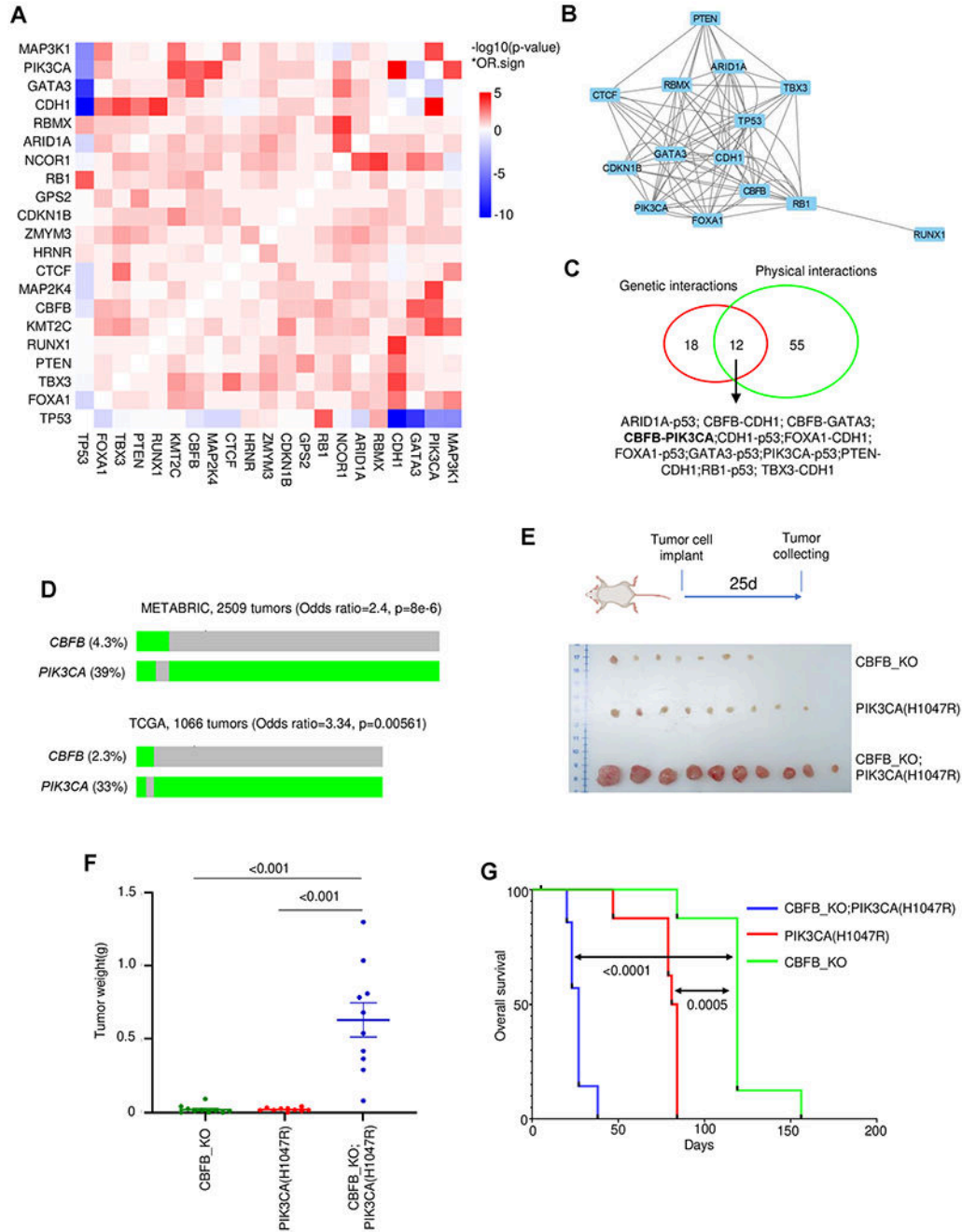
Figure 1. CBFB and PIK3CA mutations cooperate in human breast cancer.
(**A**) A matrix showing p-values (−log10 scale) of pairwise genetic interaction of top 21 mutated genes in breast tumors in the TCGA dataset. red, co-occurring; blue, mutually exclusive. OR, odds ratio. Define the OR.sign=1 if OR is > 1, and −1 if OR < 1. (**B**) A Cytoscape plot showing the interactions between the proteins encoded by the top 21 mutated genes. (**C**) A Venn diagram showing the intersection between the genetic interactions of the 21 genes and physical interactions of their proteins. (**D**) A oncoprint showing that *CBFB* and *PIK3CA* mutations co-occur in the METABRIC and TCGA datasets. Only tumors that

have either gene mutation are shown. P-values are from the Fisher Exact test. (**E and F**) Images (**E**) and weights (**F**) of subcutaneous tumors from MCF10A-derived cells in NSG mice. n=10 mice for each group. Three mice and one mouse did not have a detectable tumor for the CBFB_KO and PIK3CA(H1047R) group, respectively. p-values are from the Mann-Whitney test. (**G**) Kaplan-Meier survival curve showing the overall survival of mice bearing subcutaneous tumors. Eight mice for each group. p-values are from the log-rank (Mantel-Cox) test.
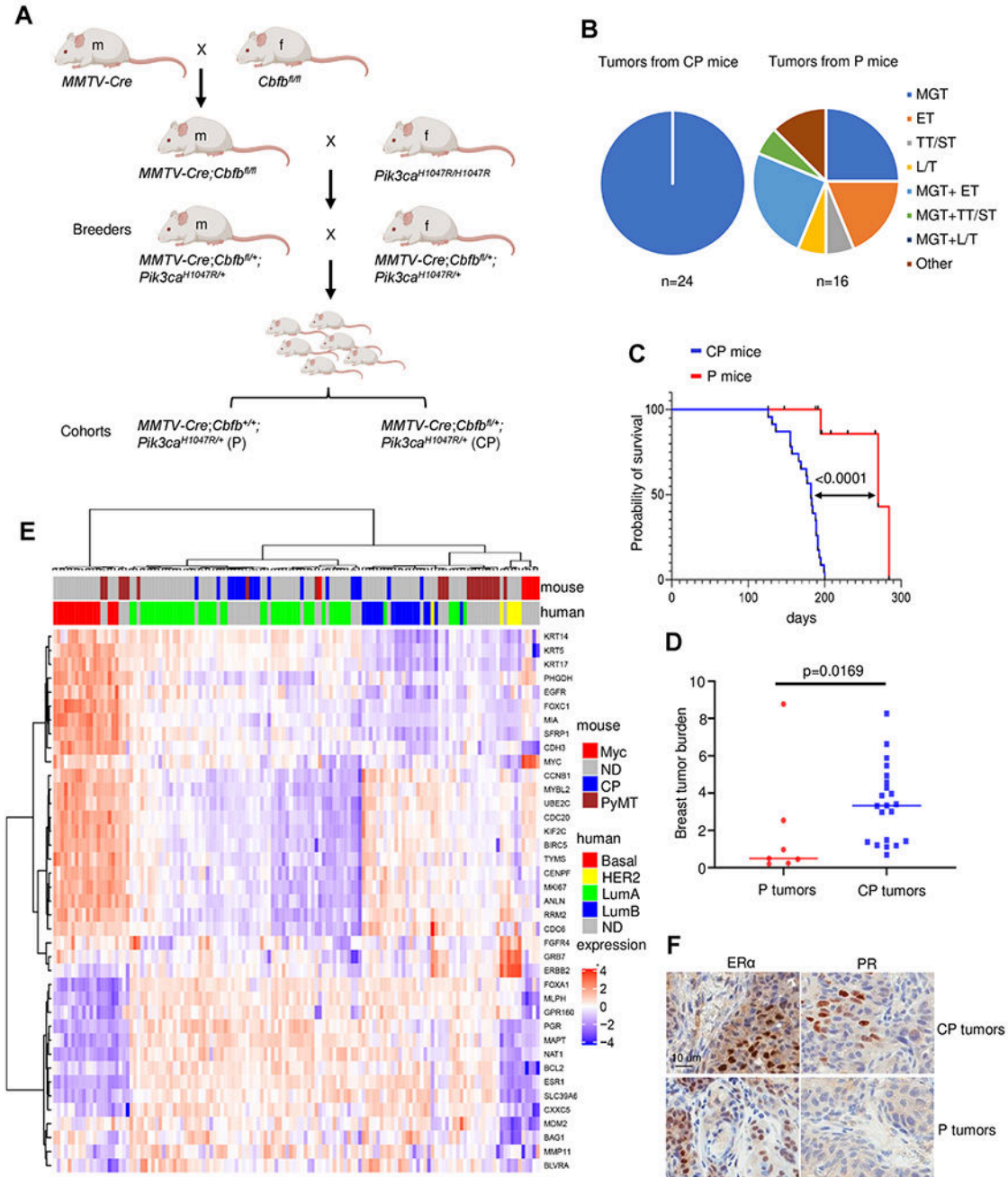
Figure 2. CBFB and PIK3CA mutations cooperate in mouse mammary tumorigenesis.
(**A**) Schematic for breeding strategy. m, male; f, female. (Created with BioRender.com)
(**B**) Spectra of spontaneous tumors from multiparous GEMMs. CP mice, *MMTV-Cre;Cbfb^{fl/+};Pik3ca^{H1047R/+}*. P mice, *MMTV-Cre;Cbfb^{+/+};Pik3ca^{H1047R/+}*. *MMTV-Cre*: MMTV-driven Cre. *Cbfb^{fl/+}* or *Cbfb^{+/+}*: heterozygous or WT *Cbfb* allele, respectively. *Pik3ca^{H1047R/+}*: heterozygous for *Pik3ca^{H1047R}* transgene in the ROSA26 locus. MGT, mammary gland tumors; ET, eye tumors; TT/ST, tail tumors or skin tumors; L/T, lymphoma or thymoma; Other, no obvious. (**C**) Kaplan-Meier survival curve showing overall survival

of GEMMs. (**D**) Tumor burden (weight sum of all tumors, grams) of each mouse. p-values are from the Mann-Whitney test. (**E**) Clustering of CP model, other mouse models, and human breast tumors using PAM50 signature. (**F**) Immunohistochemistry showing estrogen receptor alpha (ERα) and progesterone receptor (PR) expression in tumors from GEMMs.
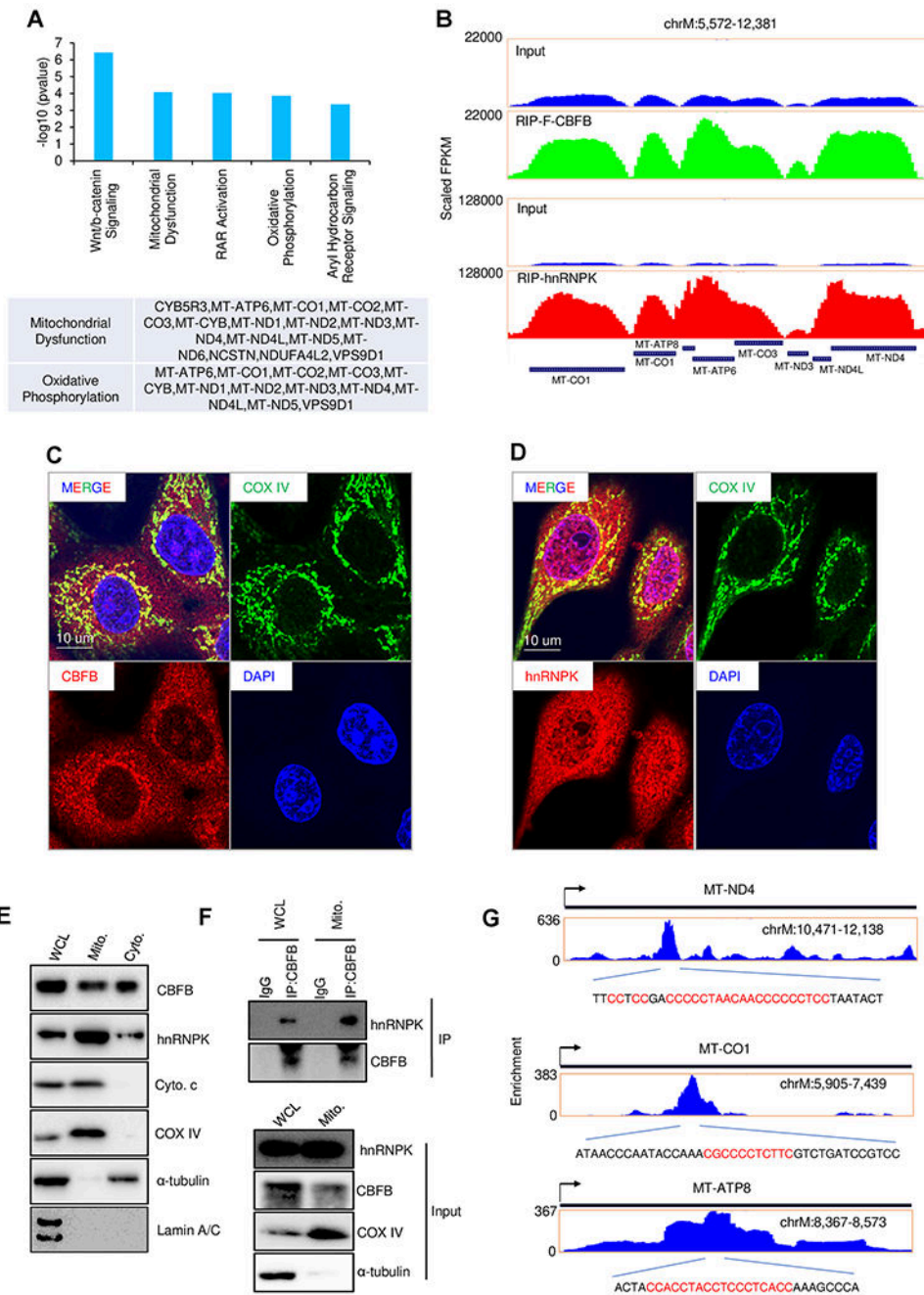
Figure 3. CBFB and its binding partner hnRNPK localize to mitochondria and bind to mitochondrially encoded mRNAs.
(**A**) IPA showing the top five enriched pathways in mRNAs bound by both CBFB and hnRNPK (data:GSE119800). (**B**) Genomic view of RIP-seq showing binding of CBFB and hnRNPK to several mt-mRNAs. (**C and D**) Immunofluorescence showing mitochondrial localization of CBFB (**C**) and hnRNPK (**D**) in MCF10A cells. (**E**) Cell fractionation showing enrichment of CBFB and hnRNPK in the mitochondrial fraction in MCF10A cells. WCL, whole cell lysate; Mito., mitochondrial; Cyto., cytosolic fraction. The same amount of

protein was loaded for each lane. (**F**) Immunoprecipitation showing the interaction of CBFB and hnRNPK in the mitochondrial fraction. (**G**) eCLIP showing hnRNPK binding sites in mt-mRNAs in K562 cells (data: GSM2423241). Red nucleotides are C-tracts.
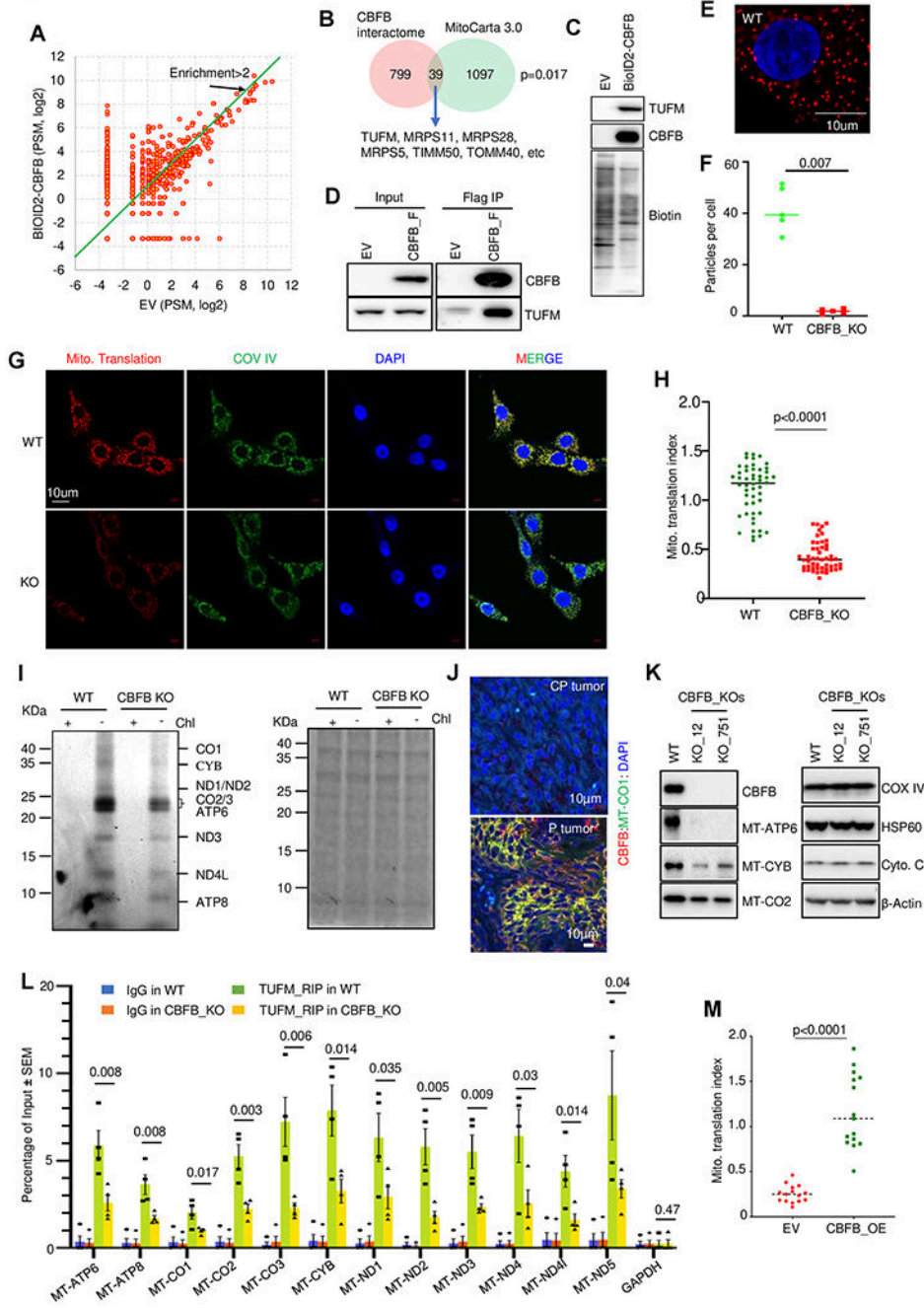
Figure 4. CBFB maintains mitochondrial translation by enhancing the binding of TUFM to mt-mRNAs.
(**A**) BioID to identify the interactome of CBFB in MCF10A cells. Each dot represents one protein. The green line indicates 2-fold enrichment (BioID2-CBFB versus EV, empty vector). Shown are the average of three biological repeats. (**B**) Venn diagram showing CBFB-bound mitochondrial proteins included in MitoCarta 3.0 (18). p-value is from the hypergeometric test. (**C**) WB of BioID pull-down validating biotinylation of TUFM. (**D**) Immunoprecipitation showing the physical interaction between CBFB and TUFM. (**E and**

F) Proximity ligation assay (PLA) showing the endogenous interaction between CBFB and TUFM in WT and CBFB_KO MCF10A cells. **E** is a representative image from two biological repeats, and **F** is five random images from these two repeats. The p-value is from the Mann-Whitney test. (**G and H**) *In situ* mitochondrial translation assay in MCF10A cells of the indicated genotypes. (**G**) A representative image for WT and CBFB_KO. (**H**) the quantification of mitochondrial translation. Shown are the average of three biological repeats. p-values are from the Mann-Whitney test. (**I**) In-gel images showing mitochondrial translation in WT and CBFB_KO MCF10A cells. Shown is the representative images of two biological repeats. Right panel shows equal loading of samples by GelCode Blue staining. (**J**) Immunofluorescence staining of CBFB (red), MT-CO1 (green), and DAPI (blue) using formalin-fixed paraffin-embedded (FFPE) slides of tumors from GEMMs. (**K**) WB showing the steady-state levels of CBFB, mitochondrially encoded proteins (MT-ATP6, MT-CYB, and MT-CO2), and non-mitochondrially encoded proteins (COX IV, HSP60, Cyto. C, and β-actin). (**L**) RNA immunoprecipitation (RIP) followed by real-time PCR showing the effect of CBFB on TUFM-mt-mRNA binding in WT and CBFB_KO MCF10A cells. p-values are from the t-test. Shown is the average of four biological repeats. (**M**) Quantification of the *in situ* mitochondrial translation assay in MCF7 cells of the indicated genotypes. Representative images are shown in Supplementary Fig. 4F. Shown are the average of three biological repeats. p-values are from the Mann-Whitney test.
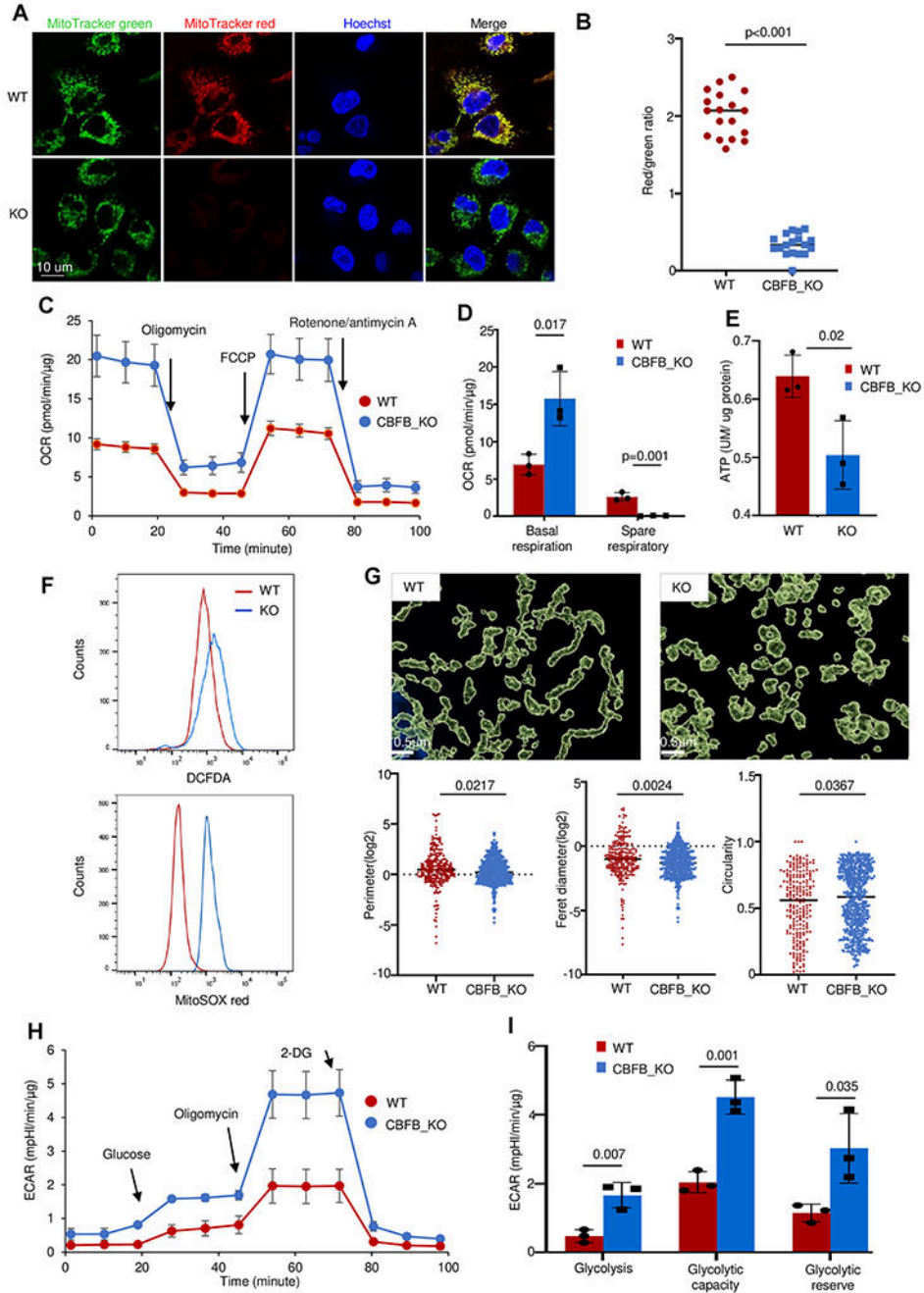
Figure 5. Mitochondrial translation defects lead to mitochondrial dysfunction, aberrant ROS levels, and aerobic glycolysis.

(**A**) Confocal images of MitoTracker Green (membrane potential-insensitive), MitoTracker Red (membrane potential-sensitive), and DAPI staining. Shown are the representative images of three biological repeats. p-values are from the t-test. (**B**) Quantification of (**A**). (**C**) Mitochondria Stress Test assay by Seahorse measuring mitochondrial function. (**D**) Basal respiration and spare respiration of WT and CBFB_KO MCF10A cells. Shown are the average of three biological repeats. p-values are from the t-test. (**E**) ATP measurement.

Shown are the average of three biological repeats. p-values are from the t-test. (**F**) Flow cytometry quantification of total (DCFDA) and mitochondrial (MitoSOX red) ROS. Shown are the representative histograms of two biological repeats (**G**) Super-resolution microscopy images and 3D reconstruction of mitochondria using COX IV staining. Upper, representative images; bottom, quantification of the perimeter, ferret diameter, and circularity of each mitochondrion. Shown are the representative images of three biological repeats. p-values are from the Mann-Whitney test. (**H**) Glycolysis Stress Test by Seahorse. (**I**) Glycolysis, glycolytic capacity, glycolytic reserve of WT and CBFB_KO MCF10A cells. Shown are the average of three biological repeats. p-values are from the t-test.
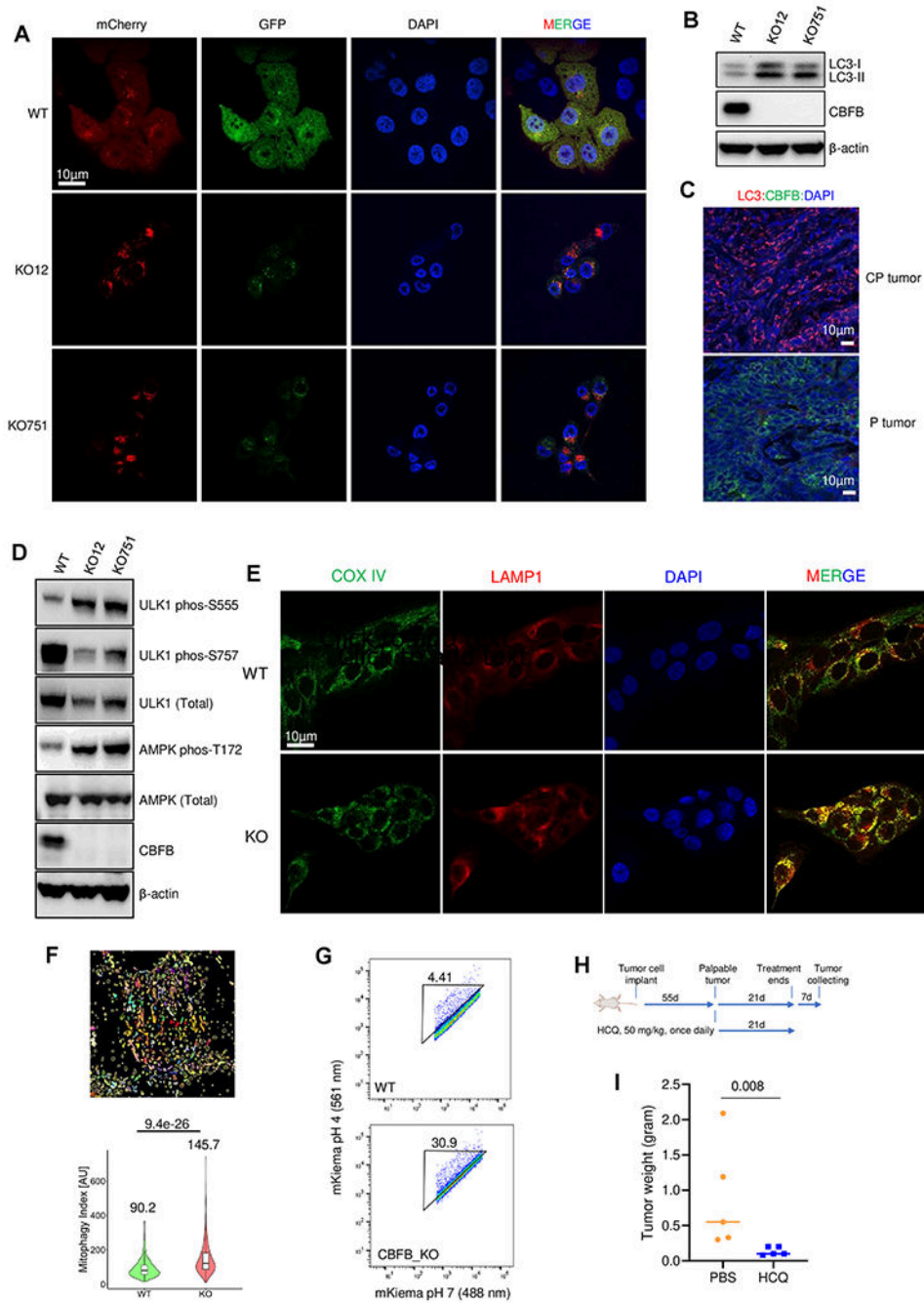
Figure 6. Mitochondrial translation defects cause enhanced autophagy and mitophagy.
(**A**) Confocal images showing autophagic flux in WT and CBFB_KO MCF10A cells. A low pH environment in lysosomes quenches the EGFP signal. Thus, a higher ratio of mCherry versus EGFP and more puncta of mCherry correlate with a higher autophagic flux. Shown are the representative images of three biological repeats. (**B**) WB of LC3-I/II, CBFB, and β-actin. (**C**) Immunofluorescence staining of LC3 (red), CBFB (green), and DAPI (blue) using FFPE slides of tumors from CP and P GEMMs. (**D**) WB showing CBFB, total and phosphorylated ULK1, and AMPK. (**E**) Immunostaining of COV IV and

LAMP1. Colocalization is indicative of mitophagy. Shown are the representative images of three biological repeats (**F**) Machine learning to estimate the mitophagy index. Left, one example showing machine learning-based segmentation of mitochondria (solid colors) and lysosomes (empty colors) in a single cell. Bottom, quantifications of mitophagy using machine learning. (**G**) mKiema assay to measure mitophagy activity in WT and CBFB_KO MCF10A cells. Mitochondrially localized mito-mKiema excites at 488 nm and 561 nm at pH 4 and pH 7, respectively. (**H**) Schematic experimental design of testing the effect of HCQ treatment on the growth of CBFB_KO MCF10A (carrying a luciferase reporter) xenografts in NSG mice. (**I**) Tumor weight on Day 28 of HCQ treatment. All p-values from this figure are from the Mann-Whitney test.
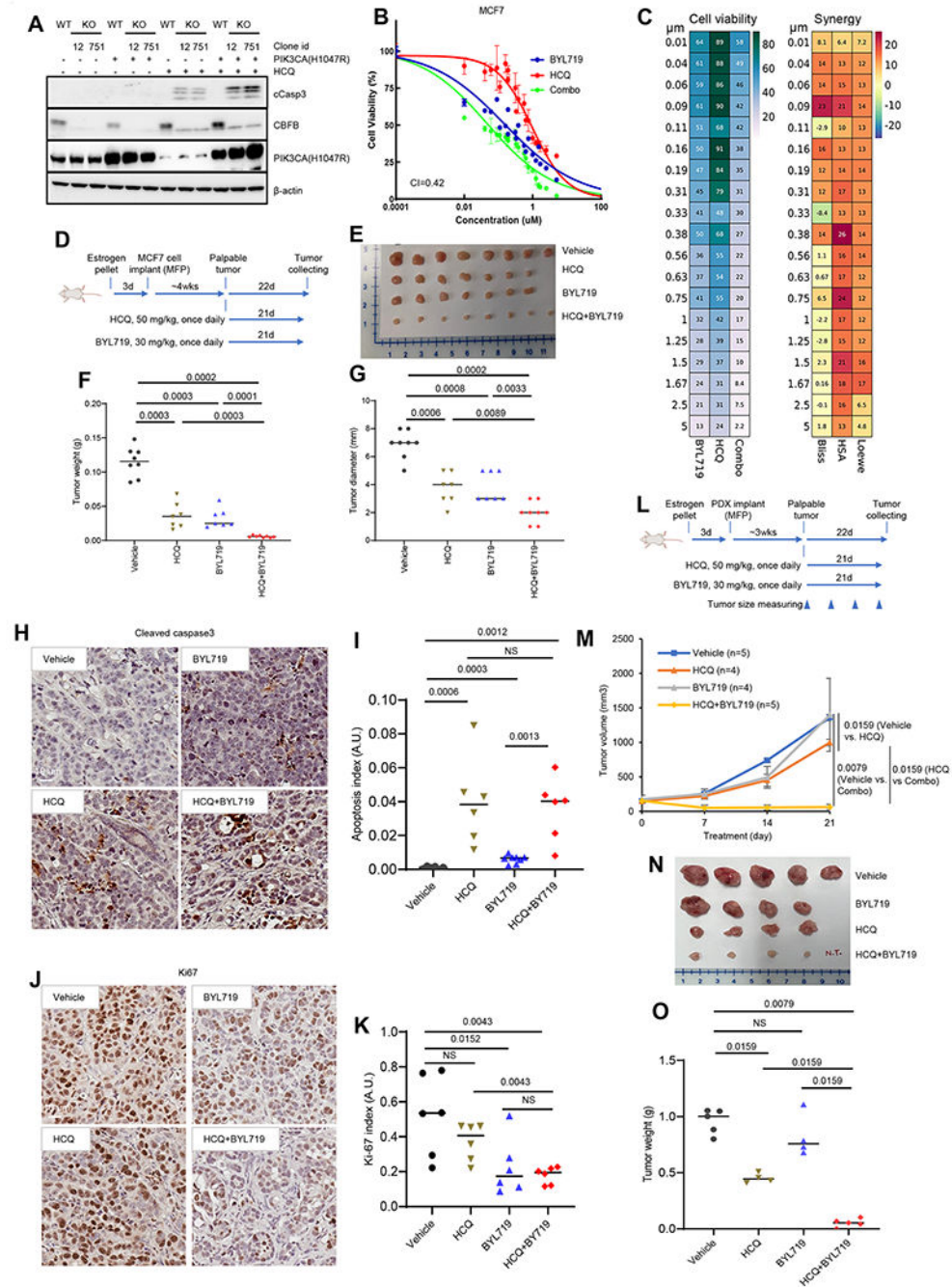
Figure 7. Synergistic effects of autophagy and PIK3CA inhibitors on breast cancer inhibition.
(**A**) WB showing the effect of HCQ on apoptosis in MCF10A cells with indicated genotypes. (**B**) Cell viability of MCF7 cells treated with HCQ or BYL719 alone or in combination at the indicated concentration for 72 hours. CI, combination index. Values less than 1 show synergy. Shown are the average of three biological repeats (**C**) Heatmaps showing cell viability and synergy score using Bliss, HAS, and Loewe algorithms. Values greater than 20 indicate synergy. Shown are the average of three biological repeats (**D**) Schematic experimental design of testing the combinatorial effect of HCQ (50 mg/kg) and

BYL719 (30 mg/kg) on MCF7 xenografts (MFP, mammary fat pad). (**E-G**) Tumor images (**E**), weight (**F**, grams), and size (**G**, mm, longest diameter) of MCF7 tumors treated with vehicle, HCQ, or BYL719 alone or in combination. (**H**) IHC showing cCasp3 staining of FFPE slides of MCF7 xenograft tumors treated with the indicated drugs. (**I**) Quantification of **H**. (**J**) IHC showing Ki-67 staining of FFPE slides of MCF7 xenograft tumors treated with the indicated drugs. (**K**) Quantification of **J**. (**L**) Schematic experimental design of testing the synergistic effect of HCQ and BYL719 on the growth of breast cancer PDX, HCI-017. (**M**) Tumor size measurement on day 0, 7, 14, and 21 of treatments. Error bars standard deviation. n is the number of mice survived at the endpoint. p-values are from the Mann-Whitney test. (**N**) Tumor images on day 22 after the first treattment. Each treatment group started with 5 mice. One mouse died in HCQ group and BYL719 group during the treatment. N.T., no tumor detected on day 22. (**O**) tumor weight (grams). All p-values in this figure are from the Mann-Whitney test.